CHALMERS | UNIVERSITY OF GOTHENBURG

MASTER'S THESIS

A Wave Propagation Solver for Computational Aero-Acoustics

ELIN SOLBERG

Department of Mathematical Sciences
Division of Mathematics
CHALMERS UNIVERSITY OF TECHNOLOGY
UNIVERSITY OF GOTHENBURG
Gothenburg, Sweden 2012

Thesis for the Degree of Master of Science

A Wave Propagation Solver for Computational Aero-Acoustics

Elin Solberg

Department of Mathematical Sciences
Division of Mathematics
Chalmers University of Technology and University of Gothenburg
SE – 412 96 Gothenburg, Sweden
Gothenburg, February 2012

Matematiska vetenskaper
Göteborg 2012

Abstract

Simulation software is increasingly replacing traditional physical testing in the process of product development, as it can in many cases reduce development times and costs. In a variety of applications, the reduction of noise is an important aspect of the product design and using methods from the field of computational aero-acoustics (CAA), the generation and propagation of sound in air may be simulated.

In this project, a FEM-based solver for the three-dimensional Helmholtz equation, modeling the propagation of sound waves, has been developed and tested. The implementation includes Galerkin/least-squares stabilization. Both interior and exterior problems are handled; the latter by a coupled finite-infinite element method. Further, using a hybrid CAA methodology the solver may be coupled to a CFD solver, to simulate the sound arising from transient fluid flows.

The solver has been tested, and observed to perform well, on a set of interior and exterior problems. Results are presented for three cases of increasing complexity: first an interior, homogeneous problem with a known analytical solution, second an exterior problem with point sources and third an exterior problem with acoustic sources from a CFD computation, i.e. a full hybrid CAA simulation. In the two latter cases, the frequencies at which standing waves appear in a pipe and a deep cavity, respectively, are compared to theoretically computed values, and are seen to be well captured by the simulations. Moreover, the results of the full CAA simulation are compared to experimental data, to which they show good resemblance.

The mathematical model, numerical methods and implementation are presented in the report along with numerical results.

Keywords: Helmholtz equation, Lighthill's analogy, computational aero-acoustics, finite element method, Galerkin/least-squares stabilization, infinite element method, computational fluid dynamics.

Acknowledgments

This work has been done at Fraunhofer-Chalmers Centre (FCC) in the department of Computational Engineering and Design. I would like to express my gratitude to my supervisor, Dr. Robert Sandboge, for his guidance through this project and for all the time he has invested into it. I also wish to thank Assoc. Prof. Fredrik Edelvik, Head of Department, for giving me the opportunity to do this work at the department.

I owe gratitude to everyone working in the department, for their readiness to help and guide me in various ways throughout the project. Many thanks go to all the people at FCC for the nice working atmosphere.

I wish to thank Prof. Stig Larsson at the department of Mathematical Sciences, Chalmers University of Technology and University of Gothenburg, for giving me helpful comments and feedback during my work on the thesis.

Finally, I want to thank my husband Olov for always loving and supporting me, my mother for encouraging and believing in me, and my Lord Jesus Christ for life.

The support of Altair, by granting a license to use AcuSolve™ [1] for the CFD computations within this Master's thesis project, is gratefully acknowledged. Further software products that have been used are: Gmsh© [17], Gnuplot© [18], MATLAB® [29], ParaView© [32], Intel® Math Kernel Library [25], and Wolfram Mathematica® [40].

Elin Solberg
Göteborg, February 2012

Contents

List of Tables

List of Figures

Nomenclature

	Latin letters
a	Sesquilinear form
a_0	Speed of sound in fluid at rest
$\boldsymbol{A}$	Matrix of the discrete FEM formulation
$\boldsymbol{b}$	Right hand side of the discrete FEM formulation
B_K	Local boundary element
d	Number of spatial dimensions ($1 \leq d \leq 3$)
E_K	Local mesh element, any dimension
E^ξ	Master element, any dimension
f	Right hand side of BVP (Sections 2–4)/Frequency (Section 6)
g	Neumann boundary value
h	Mesh size
H^ξ	3D master element
J	Jacobian matrix
k	Wave number, $k = \omega/a_0$
$\boldsymbol{K}$	Stiffness matrix
L	Linear form (Sections 2 and 3)/Length (Section 6)
L^ξ	1D master element
$\mathcal{L}$	Differential operator
$\boldsymbol{M}$	Mass matrix
N	Number of degrees of freedom
N_i	Shape function
N_r	Number of radial IE basis functions
N_s	Number of transversal IE basis functions
$\boldsymbol{n}$	Normal vector
p	Pressure
Q_K	Affine mapping
r	Radius
$\mathcal{S}$	Trial space
t	Time
T_K	Local 2D mesh element (triangle)
T^ξ	2D master element
$\boldsymbol{T}$	Lighthill's stress tensor
u	Acoustic density fluctuation (unknown to solve for)
u_D	Dirichlet boundary value
$\boldsymbol{u}$	Solution vector of the discrete FEM formulation
U_ν	Radial trial space basis function
$\boldsymbol{v}$	Fluid velocity vector
V_ν	Radial test space basis function
$\mathcal{V}$	Test space
$\boldsymbol{x}$	Spatial coordinates

Greek letters	
α	Robin boundary condition coefficient (Sections 2, 3 and 4.2.1)
α	Index (Section 4.2.2)
β	Robin boundary value (Sections 2, 3 and 4.2.1)
β	Index (Section 4.2.2)
γ	Ratio of specific heats
Γ	Boundary of Ω
δ_{ij}	Kronecker delta
λ	Acoustic wave length, $\lambda = a_0/f$
$\boldsymbol{\xi}$	Master element coordinates
ϱ	Fluid density
ϱ_0	Fluid density in fluid at rest
ϱ_a	Acoustic density fluctuation, $\varrho_\mathrm{a} = \varrho - \varrho_0$
τ	GLS stabilization parameter
$\boldsymbol{\tau}$	Viscous stress tensor
φ_i	Test space basis function
ψ_i	Trial space basis function
ω	Reduced frequency, $\omega = 2\pi f$
Ω	Spatial domain, $\Omega \subset \mathbb{R}^d$

1 Introduction

Reducing noise is an important aspect of product design in many applications. Often, noise is produced by fluid flows resulting from vibrating or rotating parts of constructions, such as the blades of a fan, a lawn mower or a wind turbine. As a part of the development of new products it would be desirable to use aero-acoustic simulations, rather than performing tests on prototypes, to predict sound pressure levels. Such a simulation must be capable of correctly computing the sound arising from fluid flows as well as the propagation of that sound. In this project a computer program, named caaHelmholtz, for the simulation of propagation of sound in three-dimensional space has been developed using a computational aero-acoustic formulation based on Lighthill's analogy [28].

Fluid flow is most generally modeled by Navier-Stokes equations. However, as pointed out in [31], it is for several reasons impractical to use these equations for simulating acoustic quantities; far from the sound source simpler equations are accurate enough to model the acoustic response, and in general the variations in acoustic quantities are small compared to variations in other flow quantities. Therefore, a highly resolved mesh would be required when solving the Navier-Stokes equations, for the acoustic variations to be accurately computed. Still, the solution of the Navier-Stokes equations computed on a coarser mesh may be accurate enough to be used as source terms, driving an equation for the sound propagation. A hybrid methodology, suggested by Oberai et al. in [31], is thus often used:

1. In a first step a computational fluid dynamics (CFD) computation is performed, solving the Navier-Stokes equations in order to obtain acoustic source terms.

2. In a second step the sound is propagated by means of a special case of the Helmholtz equation: the reduced form of Lighthill's analogy.

Using an extension to this methodology, developed by Caro et al. in [12] (see also [13, 33, 34]), it is possible to also handle moving geometries, such as fan blades. This is done by encapsulating the moving part of the geometry by an artificial surface on which surface source terms are computed in the first step (in addition to the volumetric source terms) and propagated in the second step.

Within this project, attention is focused on the second step, treating the source terms from the CFD computations as given input data. In the following section Lighthill's analogy and its reduced form - a special case of the Helmholtz equation - are derived from the Navier-Stokes equations. Further, boundary conditions, source terms and variational formulations are discussed. In Section 3, the numerical methods used in this work to solve the interior and exterior Helmholtz problems are presented and in

Section 4, the details of their implementation are given. Numerical results in one and two dimensions are presented in Section 5, results using the three-dimensional solver caaHelmholtz are given in Section 6 and the work is concluded in Section 7. In Section 8, the work that has been performed by the author and the contributions to this project of other persons are specified.

To date not many aero-acoustic simulation programs are available; notable exceptions are the ACTRAN AeroAcoustics software developed by Free Field Technologies (a part of MSC Software Corporation) and LMS Virtual.Lab Acoustics by LMS International.

2 Theory

2.1 Derivation of Lighthill's Analogy and the Helmholtz Equation

The following derivation of Lighthill's analogy and the Helmholtz equation follows the outline in [31]. We start by writing the compressible Navier-Stokes equations [38] in the form

$$\frac{\partial \varrho}{\partial t} + \nabla \cdot (\varrho \boldsymbol{v}) = 0, \tag{1a}$$

$$\frac{\partial}{\partial t}(\varrho v_i) + \sum_{j=1}^{d} \frac{\partial}{\partial x_j}(\varrho v_i v_j) = -\frac{\partial p}{\partial x_i} + \sum_{j=1}^{d} \frac{\partial \tau_{ij}}{\partial x_j} \quad \text{for } i = 1, \ldots, d, \tag{1b}$$

where ϱ is the density, $\boldsymbol{v}$ the velocity and p the pressure of the fluid, $\boldsymbol{\tau}$ is the viscous stress tensor and d is the number of spatial dimensions. By rearranging equation (1b) and adding the term $a_0^2 \frac{\partial}{\partial x_i} \varrho$ to both sides, the equation may be rewritten as

$$\frac{\partial}{\partial t}(\varrho v_i) + a_0^2 \frac{\partial}{\partial x_i} \varrho = -\sum_{j=1}^{d} \frac{\partial T_{ij}}{\partial x_j} \quad \text{for } i = 1, \ldots, d, \tag{2}$$

where $\boldsymbol{T}$ is Lighthill's turbulence tensor, defined by

$$T_{ij} = \varrho v_i v_j + \left((p - p_0) - a_0^2 (\varrho - \varrho_0) \right) \delta_{ij} - \tau_{ij}, \tag{3}$$

where δ_{ij} is the Kronecker delta, $p_0 \approx 101325\,\mathrm{Pa}$ is the average sea-level pressure, $\varrho_0 \approx 1.204\,\mathrm{kg/m^3}$ is the density of air and $a_0 \approx 343.4\,\mathrm{m/s}$ is the speed of sound in air at rest at 20°C [26]. We will consider only flows with $|\boldsymbol{v}| \ll a_0$, so that relative to the speed of sound the air is approximately at rest. Further, in isentropic flow with high Reynolds number and low Mach number, Lighthill's tensor is approximated ([12, 13]) by

$$T_{ij} \approx \varrho v_i v_j. \tag{4}$$

Subtracting the divergence of equation (2) from the time derivative of equation (1a) gives

$$\frac{\partial^2 \varrho}{\partial t^2} - a_0^2 \Delta \varrho = \sum_{i=1}^{d} \sum_{j=1}^{d} \frac{\partial^2 T_{ij}}{\partial x_i \partial x_j},$$

which is equivalent to **Lighthill's acoustic analogy**:

$$\frac{\partial^2 \varrho_{\mathrm{a}}}{\partial t^2} - a_0^2 \Delta \varrho_{\mathrm{a}} = \sum_{i=1}^{d} \sum_{j=1}^{d} \frac{\partial^2 T_{ij}}{\partial x_i \partial x_j}, \tag{5}$$

where $\varrho_{\mathrm{a}} = \varrho - \varrho_0$. Lighthill's analogy is thus formulated in terms of density fluctuations ϱ_{a}. Under the assumption of isentropic flow, however, pressure fluctuations can be readily computed from density fluctuations using the isentropic relation

$$\frac{p}{p_0} = \left(\frac{\varrho}{\varrho_0} \right)^{\gamma},$$

where γ is the ratio of specific heats[1], taking the value $\gamma = 1.402$ in air at 20°C [26].

In equation (5), the Lighthill tensor $\boldsymbol{T}$ on the right hand side depends on the unknown ϱ_{a}. If we assume that the right hand side can be decoupled from the solution we have the linear Lighthill's analogy, which is a special case of the inhomogeneous wave equation

$$\frac{\partial^2 \varrho_{\mathrm{a}}}{\partial t^2} - a_0^2 \Delta \varrho_{\mathrm{a}} = f.$$

In the (general) wave equation the right hand side $f = f(\boldsymbol{x}, t)$ may represent any sound source, whereas in Lighthill's analogy the right hand side, expressed in terms of Lighthill's tensor, represents specifically the sources generated by transient fluid flow.

The Helmholtz equation is derived from the wave equation by transformation from the time domain to the frequency domain. We assume that any real, time-dependent quantity q is periodic with period T in time, so that it may be written as a Fourier series

$$q(\mathbf{x}, t) = \mathrm{Re} \left(\sum_{n=0}^{\infty} \tilde{q}_n(\mathbf{x}) e^{i \omega_n t} \right),$$

with

$$\omega_n = \frac{2\pi n}{T}.$$

---

[1] $\gamma = C_p / C_v$, where C_p is the specific heat at constant pressure and C_v is the specific heat at constant volume [38].

The inhomogeneous wave equation then reduces to the inhomogeneous **Helmholtz equation**

$$-\Delta\tilde{\varrho}_{\mathrm{a}} - k_n^2\,\tilde{\varrho}_{\mathrm{a}} = \tilde{f} \tag{6}$$

where a_0^{-2} was absorbed in $\tilde{f}$, and $k_n = \frac{\omega_n}{a_0}$ is the acoustic wave number. Note that the Helmholtz equation is time-independent and that the frequencies ω_n are decoupled. Equation (6) can thus be solved individually for each frequency ω_n of interest. In the following we skip the index n and let k denote any wave number.

Applying the same procedure to Lighthill's analogy (5) results, analogously, in a special case of the Helmholtz equation:

$$-\Delta\tilde{\varrho}_{\mathrm{a}} - k^2\,\tilde{\varrho}_{\mathrm{a}} = \frac{1}{a_0^2}\sum_{i=1}^{d}\sum_{j=1}^{d}\frac{\partial^2\tilde{T}_{ij}}{\partial x_i\partial x_j}, \tag{7}$$

which will be referred to as the reduced form of Lighthill's analogy. Although being a special case of the Helmholtz equation, equation (7) is handled in a partly different way. In the following discussion the two equations will therefore be treated separately where needed.

2.2 Boundary Value Problems

Let us first consider the interior problem, i.e., the Helmholtz equation (or the reduced form of Lighthill's analogy) on a bounded domain Ω with boundary Γ. We will treat the Helmholtz equation (6) as a model problem with standard boundary conditions: Dirichlet, Neumann and Robin conditions. In order to simplify comparisons to standard literature, we substitute the name of the unknown, $\tilde{\varrho}_{\mathrm{a}}$, by the more common name u. We thus have the boundary value problem (BVP)

$$\begin{array}{ll} -\Delta u - k^2 u = \tilde{f} & \text{in } \Omega, \\ u = u_{\mathrm{D}} & \text{on } \Gamma_{\mathrm{D}}, \\ \frac{\partial u}{\partial n} = g & \text{on } \Gamma_{\mathrm{N}}, \\ \alpha u + \frac{\partial u}{\partial n} = \beta & \text{on } \Gamma_{\mathrm{R}}, \end{array} \tag{8}$$

where $\Gamma_{\mathrm{D}}, \Gamma_{\mathrm{N}}$ and Γ_{R} are subsets of Γ and $u_{\mathrm{D}}, g, \alpha$ and β are given on the corresponding parts of the boundary. (Of course, the Neumann condition can also be considered a special case of the Robin condition, with $\alpha = 0$.)

In the case of the reduced form of Lighthill's analogy, we write the BVP as

$$-\Delta u - k^2 u = \frac{1}{a_0^2}\sum_{i=1}^{d}\sum_{j=1}^{d}\frac{\partial^2\tilde{T}_{ij}}{\partial x_i\partial x_j} \quad \text{in } \Omega, \tag{9a}$$

$$\frac{\partial u}{\partial n} = -\frac{1}{a_0^2}\sum_{i=1}^{d}\sum_{j=1}^{d}\frac{\partial\tilde{T}_{ij}}{\partial x_j}n_i \quad \text{on } \Gamma, \tag{9b}$$

where the Neumann condition (9b) represents a solid boundary, where the surface of the computational domain is fixed and sound is completely reflected, see [31].

The right hand side of equation (9a) is interpreted as a volumetric source term, accounting for sound generated by transient fluid flow within the computational domain. The source is modeled by the divergence of Lighthill's turbulence tensor $\mathbf{T}$, which is computed from the results of the CFD computation and hence regarded as given in (9a). The quantity $\varrho_{\mathrm{a}} = \varrho - \varrho_0$ present in expression (3) for $\mathbf{T}$ is thus interpreted as known and distinct from the unknown acoustic density for which we are solving the BVP, which is the standard interpretation of Lighthill's analogy [31].

We have so far assumed Ω to be bounded. It is, however, often necessary to consider exterior rather than interior problems, in which case Ω is unbounded. The solution must then satisfy the Sommerfeld radiation condition

$$\lim_{|x|\to\infty} |x|^{\frac{d-1}{2}} \left(\frac{\partial u}{\partial |x|} - iku \right) = 0, \tag{10}$$

to assure, for one thing, correct decay behavior at a large distance from the sources, and for another, radiation only towards - not from - infinity [24].

2.3 Variational Formulations

We will now discuss the variational formulations of the boundary value problems (8) and (9) and of their counterparts on an unbounded domain. As before we consider first the case of a bounded domain.

2.3.1 Interior Problems

For the variational formulation of the Helmholtz problem (8), on a bounded domain Ω, we define a trial space

$$\mathcal{S} := \{u \in H^1(\Omega) : u|_{\Gamma_{\mathrm{D}}} = u_{\mathrm{D}}\},$$

imposing the Dirichlet boundary condition explicitly on the trial solutions. Here we let functions in $H^1(\Omega)$ be complex-valued. We also define a test space

$$\mathcal{V} := \{v \in H^1(\Omega) : v|_{\Gamma_{\mathrm{D}}} = 0\},$$

with functions vanishing on the Dirichlet part of the boundary. The variational form can then be written (see, e.g., [24]) as: Find $u \in \mathcal{S}$ such that

$$a(u,v) = L_{\mathrm{H}}(v) \quad \forall v \in \mathcal{V},$$

where

$$a(u,v) := \int_\Omega \left(\nabla u \cdot \nabla \bar{v} - k^2 u \bar{v} \right) \, \mathrm{d}\Omega + \int_{\Gamma_{\mathrm{R}}} \alpha u \bar{v} \, \mathrm{d}\Gamma, \tag{11}$$

and

$$L_{\mathrm{H}}(v) := \int_{\Omega} \tilde{f}\bar{v}\,\mathrm{d}\Omega + \int_{\Gamma_{\mathrm{R}}} \beta\bar{v}\,\mathrm{d}\Gamma + \int_{\Gamma_{\mathrm{N}}} g\bar{v}\,\mathrm{d}\Gamma, \tag{12}$$

with the bar over v denoting complex conjugate. We use the subscript H to denote the right hand side of the variational (regular) Helmholtz problem. For the reduced form of Lighthill's analogy we will use the subscript L.

A variational formulation of Lighthill's analogy was first derived by Oberai et al. in [31]. It differs from the treatment of the Helmholtz BVP (8) in that Green's theorem is applied not only to the term including the Laplacian, but also to the right hand side of equation (9a). With some abuse of notation we then write the variational formulation: Find $u \in H^1(\Omega)$ such that

$$a(u,v) = L_{\mathrm{L}}(v) \quad \forall v \in H^1(\Omega),$$

where we let a be defined as in (11), but under the assumption that now no Robin condition is imposed, so that $\Gamma_{\mathrm{R}} = \emptyset$ and hence only the integral over Ω remains. Further,

$$L_{\mathrm{L}}(v) := -\frac{1}{a_0^2}\sum_{i=1}^{d}\sum_{j=1}^{d}\int_{\Omega}\frac{\partial\tilde{T}_{ij}}{\partial x_j}\frac{\partial\bar{v}}{\partial x_i}\,\mathrm{d}\Omega + \frac{1}{a_0^2}\sum_{i=1}^{d}\sum_{j=1}^{d}\int_{\Gamma}\frac{\partial\tilde{\Sigma}_{ij}}{\partial x_j}n_i\bar{v}\,\mathrm{d}\Gamma, \tag{13}$$

with $\tilde{\Sigma}_{ij}$ being the reduced form of Σ_{ij}, defined by

$$\Sigma_{ij} := \varrho v_i v_j + (p - p_0)\delta_{ij} - \tau_{ij} = T_{ij} + a_0^2\varrho_{\mathrm{a}}\delta_{ij}.$$

If all boundaries are solid, the integral over Γ in (13) vanishes due to the boundary condition (9b).

A novel interpretation of the boundary integral was introduced by Caro et al. in [12] (see also [13, 33, 34]) and extends the model to moving geometries. This is achieved by encapsulating the moving parts of the geometry by an artificial surface, on which $\tilde{\Sigma}_{ij}$ can be computed from the results of the CFD computation. The volume inside the encapsulating surface is thus part of the CFD domain, but not of the acoustic computational domain. The boundary integral is then interpreted as a surface source term, accounting for sound sources inside the encapsulated volume.

2.3.2 Exterior Problems

For exterior problems, where integration is performed over the unbounded domain Ω, care must be taken to choose trial and test spaces such that the integrals in the variational formulation exist. Further, the variational formulation must include the Sommerfeld radiation condition (10). We follow here the choice of function spaces presented in [24] (Section 2.3.2).

For exterior problems we assume that the support of volumetric sources (i.e., the right hand side of the Helmholtz equation and the reduced form of

Lighthill's analogy, respectively) is bounded and that Γ is the outer boundary of an object of finite volume, the exterior of which is Ω.

It has been shown (see [4, 39]) that any solution to the three-dimensional, homogeneous Helmholtz equation satisfying the Sommerfeld radiation condition can be expanded as a series, the Wilcox-Atkinson expansion, in spherical coordinates $\boldsymbol{r} = (r, \theta, \phi)$:

$$u(\boldsymbol{r}) = \frac{e^{ikr}}{r} \sum_{n=0}^{\infty} \frac{u_n(\theta, \phi)}{r^n}. \tag{14}$$

The asymptotic dependence of the solution on r is thus e^{ikr}/r, which is not in $H^1(\Omega)$. A different choice of trial and test spaces is thus needed. Therefore we introduce two weighted inner products

$$\begin{aligned}(u, v)_w &:= \int_\Omega w\, u\bar{v}\, \mathrm{d}\Omega, \quad w := r^{-2},\\ (u, v)_{w^*} &:= \int_\Omega w^*\, u\bar{v}\, \mathrm{d}\Omega, \quad w^* := r^2,\end{aligned}$$

and the associated norms

$$\begin{aligned}\|u\|_{1,w} &:= ((u, u)_w + (\nabla u, \nabla u)_w)^{1/2},\\ \|u\|_{1,w^*} &:= ((u, u)_{w^*} + (\nabla u, \nabla u)_{w^*})^{1/2},\end{aligned}$$

inducing the function spaces

$$H^1_w(\Omega) := \{u : \|u\|_{1,w} < \infty\},$$

and

$$H^1_{w^*}(\Omega) := \{u : \|u\|_{1,w^*} < \infty\}.$$

As e^{ikr}/r belongs to $H^1_w(\Omega)$, this is a natural candidate for a trial space. Further, with $u \in H^1_w(\Omega)$ and $v \in H^1_{w^*}(\Omega)$ it can be shown using the Cauchy-Schwarz inequality that the integrals

$$\int_\Omega u\bar{v}\, \mathrm{d}\Omega \quad \text{and} \quad \int_\Omega \nabla u \cdot \nabla \bar{v}\, \mathrm{d}\Omega$$

are finite, so that $H^1_{w^*}(\Omega)$ can be chosen as test space.

The Sommerfeld radiation condition is explicitly imposed on the solution by adding a constraint to the trial space, thus defining a new trial space:

$$\mathcal{S}_{\text{ext}} := \left\{ u \in H^1_w(\Omega) : \int_\Omega \left| \frac{\partial u}{\partial r} - iku \right|^2 \mathrm{d}\Omega < \infty \right\}.$$

Choosing now $\mathcal{V}_{\text{ext}} = H^1_{w^*}(\Omega)$ as the test space, the variational formulation of the Helmholtz equation and of the reduced form of Lighthill's analogy can be stated as in Section 2.3.1, replacing the trial and test spaces by $\mathcal{S}_{\text{ext}}$ and $\mathcal{V}_{\text{ext}}$, respectively. The volume integrals in L_{H} and L_{L} and the boundary integrals are clearly finite, since we have assumed that the volumetric sources have bounded support and that Γ is of finite measure. For a more in-depth discussion on the choice of function spaces refer to [24].

3 Numerical Methods

The variational formulations stated in Section 2.3 form the basis of the numerical methods that have been implemented; the finite element method (FEM) for interior problems and the coupled finite-infinite element method (FEM-IEM) for exterior problems. In the following, two FEM formulations and one FEM-IEM formulation are presented. Additionally an alternative to FEM-IEM for exterior problems, FEM with absorbing boundary conditions, is briefly discussed.

3.1 Interior Problems: Finite Element Methods

3.1.1 Standard Galerkin Formulation

Consider a partition of the *bounded* computational domain Ω and let $\tilde{\Omega}$ be the union of interiors of the finite elements. Let $\mathcal{S}^h \subset H^1(\Omega)$ and $\mathcal{V}^h \subset H^1(\Omega)$ be two N-dimensional finite element function spaces, consisting of piecewise polynomials on the partition. If Dirichlet conditions are prescribed on a part of the boundary Γ, then the function spaces should be modified accordingly, see Section 2.3.1. The standard Galerkin formulation of the boundary value problems (8) and (9) can then be written as: Find $u^h \in \mathcal{S}^h$ such that

$$a(u^h, v^h) = L(v^h), \quad \forall v^h \in \mathcal{V}^h, \tag{15}$$

where the sesquilinear form a is defined by (11) and the linear form L is L_{H}, defined by (12), or L_{L}, defined by (13), respectively for the two problems.

Letting $\{\psi_i\}_{i=1}^N$ be a basis for $\mathcal{S}^h$ and $\{\varphi_i\}_{i=1}^N$ a basis for $\mathcal{V}^h$ we may write the solution u^h as

$$u^h(\boldsymbol{x}) = \sum_{j=1}^{N} u_j \psi_j(\boldsymbol{x}),$$

and rewrite equation (15) in discrete form as

$$\boldsymbol{A}\boldsymbol{u} = \boldsymbol{b},$$

where $b_i = L(\varphi_i)$ and $A_{ij} = a(\psi_j, \varphi_i)$. In the absence of Robin boundary conditions we have

$$\boldsymbol{A} = \boldsymbol{K} - k^2\boldsymbol{M},$$

i.e., $\boldsymbol{A}$ is a linear combination of the mass matrix $\boldsymbol{M}$ with

$$M_{ij} = \int_{\Omega} \bar{\varphi}_i \psi_j \,\mathrm{d}\Omega,$$

and the stiffness matrix $\boldsymbol{K}$ with

$$K_{ij} = \int_{\Omega} \nabla\bar{\varphi}_i \cdot \nabla\psi_j \,\mathrm{d}\Omega.$$

3.1.2 Galerkin/Least-Squares Formulation

The standard Galerkin method is known to produce solutions of inaccurate phase and magnitude when applied to the Helmholtz equation. A remedy proposed in [19, 20] and further developed in [36] is the Galerkin/least-squares (GLS) method, in which a term, including the residual of the original Helmholtz equation (6) integrated over the finite element interiors, is added to the standard Galerkin formulation. By including the residual in the added term, the GLS method is - just like the standard Galerkin method - consistent in the sense that a solution satisfying the weak variational formulation of the Helmholtz equation also satisfies the GLS formulation.

Defining the differential operator $\mathcal{L}$ by

$$\mathcal{L}(u) := -\Delta u - k^2 u,$$

the GLS method for the Helmholtz equation can be stated as: Find $u^h \in \mathcal{S}^h$ such that

$$\begin{aligned} a(u^h, v^h) &+ \int_{\tilde{\Omega}} \mathcal{L}(u^h)\tau\mathcal{L}(\bar{v}^h)\,\mathrm{d}\tilde{\Omega} \\ &= L_{\mathrm{H}}(v^h) + \int_{\tilde{\Omega}} \tilde{f}\tau\mathcal{L}(\bar{v}^h)\,\mathrm{d}\tilde{\Omega}, \quad \forall v^h \in \mathcal{V}^h, \end{aligned} \tag{16}$$

where τ is a local parameter characterizing the GLS method, and should be computed individually for each element. The sesquilinear form a and the linear form L_{H} are defined as in Section 2.3.1. The GLS method for the reduced form of Lighthill's analogy is obtained by substituting L_{L} for L_{H} and the expression

$$\frac{1}{a_0^2}\sum_{i=1}^{d}\sum_{j=1}^{d}\frac{\partial^2 \tilde{T}_{ij}}{\partial x_i \partial x_j}$$

for $\tilde{f}$ in (16).

In [20], it is shown that for the one-dimensional problem, computing τ by

$$\tau k^2 = 1 - \frac{C_1}{(kh)^2}\frac{1-\cos(C_2 kh)}{2+\cos(C_2 kh)}, \tag{17}$$

with $C_1 = 6$ and $C_2 = 1$, leads to a nodally exact solution for any mesh resolution. Here h is the local element size.

A general suggestion for the two-dimensional case using a triangular mesh was developed in [21], a special case of which takes the form (17) with $C_1 = 8$ and $C_2 = \sqrt{3}/2$. The element size h is now defined as the average side length of the element.

In the current work, the parameters suggested for the two-dimensional case were used also for the implementation of the three-dimensional solver.

The discrete form of the GLS method can be written as

$$\boldsymbol{A}^{\mathrm{GLS}}\boldsymbol{u} = \boldsymbol{b}^{\mathrm{GLS}},$$

where

$$A_{ij}^{\mathrm{GLS}} = A_{ij} + \int_{\tilde{\Omega}} \mathcal{L}(\bar{\varphi}_i)\tau\mathcal{L}(\psi_j)\,\mathrm{d}\tilde{\Omega}. \tag{18}$$

For the Helmholtz equation

$$b_i^{\mathrm{GLS}} = b_i + \int_{\tilde{\Omega}} \tilde{f}\tau\mathcal{L}(\bar{\varphi}_i)\,\mathrm{d}\tilde{\Omega}, \tag{19}$$

while for the reduced form of Lighthill's analogy

$$b_i^{\mathrm{GLS}} = b_i + \int_{\tilde{\Omega}} \frac{1}{a_0^2}\sum_{i=1}^{d}\sum_{j=1}^{d}\frac{\partial^2\tilde{T}_{ij}}{\partial x_i\partial x_j}\tau\mathcal{L}(\bar{\varphi}_i)\,\mathrm{d}\tilde{\Omega}. \tag{20}$$

Note that for a piecewise linear function u on $\tilde{\Omega}$, $\mathcal{L}(u)$ reduces to $-k^2u$ and in the case of piecewise linear trial and test functions (18) consequently reduces (in the absence of Robin conditions, for ease of notation) to

$$\boldsymbol{A}^{\mathrm{GLS}} = \boldsymbol{K} - k^2(1-\tau k^2)\boldsymbol{M}.$$

Similarly, the integral in (19) adds no complexity to the computation of the right hand side vector $\boldsymbol{b}$; the volume integral in (12) is merely multiplied by the coefficient $(1-\tau k^2)$.

In the case of Lighthill's analogy, however, the GLS method requires additional computations even for piecewise linear trial and test functions, since the added integral in (20) is not present in the right hand side vector of the standard Galerkin formulation.

3.2 Exterior Problems

We now turn again to exterior problems, which can be computationally more challenging than interior ones. Standard spatial finite elements can be used only on a finite domain, thus when using such a method for an exterior problem, the unbounded domain Ω has to be truncated by an artificial boundary, say Γ_{r_0}, enclosing any physical boundaries, control surfaces and sources, see Section 2.2. The FEM is then used on the part of Ω that is inside Γ_{r_0} - let us denote it by Ω_{r_0} - and the boundary Γ_{r_0} should be treated in such a way that the Sommerfeld radiation condition is fulfilled (at least approximately) at infinity. This corresponds to the intuitive condition that no reflections are allowed at the artificial boundary.

Two different approaches are presented in the next two sections; first briefly the use of absorbing boundary conditions at the truncating boundary; second the coupling of infinite elements to the finite elements at the truncating boundary. Both approaches are presented for the case of Γ_{r_0} being a circle (in two dimensions) or a sphere (in three dimensions) of radius r_0.

3.2.1 Absorbing Boundary Conditions

When using absorbing boundary conditions (ABCs), the Sommerfeld condition is approximately imposed at Γ_{r_0} by the boundary condition

$$\frac{\partial u}{\partial n} = Bu \qquad \text{on } \Gamma_{r_0},$$

where the operator B is an approximation of the operator, the so-called Dirichlet-to-Neumann operator, which maps the Sommerfeld radiation condition exactly to the truncating boundary.

The ABC is characterized by the choice of the approximate operator B and a variety of such operators have been suggested in the literature. In [35], the ABCs (of low orders) suggested by Feng [16], Engquist and Majda [14, 15] and Bayliss and Turkel [6] are compared and it is concluded that in the cases tested the highest accuracy is achieved when using the Bayliss and Turkel ABCs. A zeroth order ABC is obtained formally only with the approach of Feng. Here, that zeroth order condition and the Bayliss and Turkel ABCs of first order will be presented.

The simplest possible ABC is the Sommerfeld condition applied directly at the truncating boundary rather than at infinity:

$$\frac{\partial u}{\partial n} - iku = 0 \qquad \text{on } \Gamma_{r_0},$$

i.e., the operator B is just the constant ik. This is the zeroth order Feng condition, and the formulation is the same for one, two and three spatial dimensions. In one dimension, this is the exact Dirichlet-to-Neumann operator.

The first order Bayliss and Turkel boundary condition in two dimensions is given by

$$\frac{\partial u}{\partial n} - \left(ik - \frac{1}{2r_0} \right) u = 0 \qquad \text{on } \Gamma_{r_0},$$

and in three dimensions by

$$\frac{\partial u}{\partial n} - \left(ik - \frac{1}{r_0} \right) u = 0 \qquad \text{on } \Gamma_{r_0}.$$

In a FEM setting, these low order ABCs are readily implemented as Robin conditions and do not influence the size of the system of linear equations to be solved (as does, as we shall see, the use of higher order infinite elements). High accuracy can be achieved either by using high order ABCs or by placing the truncating boundary far from the scattering objects and sources ([37]), i.e., by choosing r_0 to be large. However, only low order ABCs can be coupled to linear finite elements, so that in order to achieve high accuracy, only the latter is an alternative. This leads to a large FEM domain which in turn results in high computational cost.

In the next section an alternative to ABCs, the infinite element method, is presented. Its implementation is more involved than that of the presented ABCs, the problem size increases with the order of the infinite elements and for high orders the matrix may become ill-conditioned. A benefit, however, is that higher order schemes may be combined with linear finite elements, which is not the case when using ABCs.

3.2.2 Coupled Finite-Infinite Element Method

The general idea of the coupled finite-infinite element method (FEM-IEM) is very similar to the concept of the FEM; it is based on a variational formulation of the boundary value problem and the numerical solution is sought in a finite dimensional function space $\mathcal{S}^h_{\text{ext}}$ on Ω. The FEM is used on the bounded domain Ω_{r_0}, the part of Ω enclosed by Γ_{r_0} while the IEM is used on the unbounded domain $\Omega^+_{r_0} := \Omega \backslash \Omega_{r_0}$. We will consider only the three-dimensional case with Ω_{r_0} being the interior of a sphere with radius r_0.

A standard FEM discretization is used for Ω_{r_0}, on which regular finite-dimensional trial and test spaces $\mathcal{S}^h(\Omega_{r_0})$ and $\mathcal{V}^h(\Omega_{r_0})$ are defined. The infinite element (IE) domain $\Omega^+_{r_0}$ is discretized by a layer of elements of infinite extension in the radial direction and suitable finite-dimensional IE trial and test spaces $\mathcal{S}^{h,N_\text{r}}(\Omega^+_{r_0})$ and $\mathcal{V}^{h,N_\text{r}}(\Omega^+_{r_0})$ must be chosen. Having these function spaces, the total FEM-IEM trial and test spaces are defined by

$$\mathcal{S}^h_{\text{ext}} = \{u \in C^0;\ u|_{\Omega_{r_0}} \in \mathcal{S}^h(\Omega_{r_0}),\ u|_{\Omega^+_{r_0}} \in \mathcal{S}^{h,N_\text{r}}(\Omega^+_{r_0})\}, \tag{21}$$

$$\mathcal{V}^h_{\text{ext}} = \{u \in C^0;\ u|_{\Omega_{r_0}} \in \mathcal{V}^h(\Omega_{r_0}),\ u|_{\Omega^+_{r_0}} \in \mathcal{V}^{h,N_\text{r}}(\Omega^+_{r_0})\}. \tag{22}$$

The condition $u \in C^0$ ensures continuity over Γ_{r_0} and thereby couples the finite to the infinite elements.

An IEM formulation is characterized by the choice of IE trial and test spaces. The trial space can be written on a general form as a tensor product of two function spaces:

$$\mathcal{S}^{h,N_\mathrm{r}}(\Omega_{r0}^+) = \mathrm{span}\{U_\nu\}_{\nu=1}^{N_\mathrm{r}} \times \mathcal{S}^h(\Gamma_{r0}), \tag{23}$$

where U_ν are radial basis functions defined for $r \in [r_0, \infty)$ and $\mathcal{S}^h(\Gamma_{r0})$ is the restriction of $\mathcal{S}^h(\Omega_{r0})$ to Γ_{r0}. The trial functions can thus be written as

$$u^{h,N_\mathrm{r}}(r, \boldsymbol{s}) = \sum_{\mu=1}^{N_\mathrm{s}} \sum_{\nu=1}^{N_\mathrm{r}} c_{\mu\nu} U_\nu(r) u_\mu^h(\boldsymbol{s}),$$

where u_μ^h are basis functions matching the finite element (FE) trial space on Γ_{r0}, N_s denotes the number of such basis functions and $\boldsymbol{s}$ is a two-dimensional parametrization of Γ_{r0}.

Motivated by the Atkinson-Wilcox expansion (14), the radial basis functions U_ν are chosen as

$$U_\nu(r) = P_\nu(r_0/r) e^{ik(r-r_0)}, \qquad \nu = 1, \ldots, N_\mathrm{r},$$

where P_ν is a polynomial of degree ν. It is shown in [2] that the choice of polynomials may influence the matrix condition number, and that low condition numbers can be achieved with, e.g., shifted Legendre polynomials. For simplicity we use monomials in the current implementation, i.e.,

$$U_\nu(r) = \frac{e^{ik(r-r_0)}}{(r/r_0)^\nu}, \qquad \nu = 1, \ldots, N_\mathrm{r}. \tag{24}$$

The IE test space is chosen, analogously to the trial space (23), as

$$\mathcal{V}^{h,N_\mathrm{r}}(\Omega_{r0}^+) = \mathrm{span}\{V_\nu\}_{\nu=1}^{N_\mathrm{r}} \times \mathcal{V}^h(\Gamma_{r0}),$$

where $\mathcal{V}^h(\Gamma_{r0})$ is the restriction of $\mathcal{V}^h(\Omega_{r0})$ to Γ_{r0} and the radial basis functions V_ν must be chosen such that all integrals in the discrete formulation converge.

Infinite element schemes are commonly divided into two categories: conjugated and unconjugated formulations, depending on the choice of basis for the test space. In conjugated formulations, the test space basis is the complex conjugate of the trial space basis, possibly multiplied by a real valued factor. In unconjugated formulations, the test space basis equals the trial space basis, up to scaling by a real valued factor.

In Table 3.1, references for a few popular IE formulations - the conjugated and unconjugated Burnett and Leis formulations - are listed. The unconjugated Burnett formulation is also referred to as the Bettess-Burnett unconjugated formulation and the conjugated Leis formulation as the Astley-Leis conjugated formulation.

In [24], the conjugated Leis formulation, and the conjugated and unconjugated Burnett formulations are compared, and it is concluded that the unconjugated version converges much more rapidly in the FE domain, whereas the conjugated formulations are more accurate in the IE domain. A benefit of the conjugated formulations concerning implementation is the great simplification of the integrals to be computed that results from conjugating the test functions.

For the implementation, the Astley-Leis conjugated formulation, corresponding to the variational formulation stated in Section 2.3.2, was chosen. For the Astley-Leis formulation, the trial and test spaces are defined as in (21) and (22), respectively. The radial basis functions are defined by (24) for the trial space and by

$$V_\nu(r) = \frac{e^{ik(r-r_0)}}{(r/r_0)^\nu}, \qquad \nu = 3, \ldots, N_\mathrm{r}+2.$$

for the test space, and it follows that $\mathcal{S}^h_\mathrm{ext} \subset \mathcal{S}_\mathrm{ext}$ and $\mathcal{V}^h_\mathrm{ext} \subset \mathcal{V}_\mathrm{ext}$, where $\mathcal{S}_\mathrm{ext}$ and $\mathcal{V}_\mathrm{ext}$ are the weighted Sobolev spaces defined in Section 2.3.2. Hence the trial functions satisfy the Sommerfeld radiation condition and the integrals in the discrete formulation converge.

The coupled FEM-IEM formulation is: Find $u^{h,N_\mathrm{r}} \in \mathcal{S}^h_\mathrm{ext}$ such that

$$a(u^{h,N_\mathrm{r}}, v^{h,N_\mathrm{r}}) = L(v^{h,N_\mathrm{r}}), \qquad \forall v^{h,N_\mathrm{r}} \in \mathcal{V}^h_\mathrm{ext}, \tag{25}$$

with a as in (11) and L as in (12) for the Helmholtz problem or (13) for the reduced form of Lighthill's analogy.

Recall that the truncating boundary was chosen with a large enough radius r_0, so that there are no sources nor objects in $\Omega^+_{r_0}$. The right hand side of (25) can thus be computed as in the FEM case and the left hand side can be written, separating integrals over $\Omega^+_{r_0}$ from those over Ω_{r_0}, as

$$\begin{aligned} a(u^{h,N_\mathrm{r}}, v^{h,N_\mathrm{r}}) = &\int_{\Omega_{r_0}} \left(\nabla u^{h,N_\mathrm{r}} \cdot \nabla \bar{v}^{h,N_\mathrm{r}} - k^2 u^{h,N_\mathrm{r}} \bar{v}^{h,N_\mathrm{r}}\right) \mathrm{d}\Omega \\ &+ \int_{\Omega^+_{r_0}} \left(\nabla u^{h,N_\mathrm{r}} \cdot \nabla \bar{v}^{h,N_\mathrm{r}} - k^2 u^{h,N_\mathrm{r}} \bar{v}^{h,N_\mathrm{r}}\right) \mathrm{d}\Omega \\ &+ \int_{\Gamma_\mathrm{R}} \alpha u^{h,N_\mathrm{r}} \bar{v}^{h,N_\mathrm{r}} \, \mathrm{d}\Gamma. \end{aligned} \tag{26}$$

Table 3.1: A few popular IE formulations, categorized by choice of radial test functions.

	Burnett (Bubnov-Galerkin) $V_\nu(r) = U_\nu(r)$	Leis (Petrov-Galerkin) $V_\nu(r) = (r_0/r)^2 U_\nu(r)$
Conjugated	[9, 10, 11]	[3, 27]
Unconjugated	[7, 8, 9, 10, 11]	[24, 27]

Evaluation of the first of the above volume integrals is performed in Section 4.2.1 for the case of piecewise linear basis functions and evaluation of the second is performed in Section 4.2.2 in the case of Astley-Leis radial basis functions.

4 Implementation

We now turn to the implementation of the numerical methods discussed in the previous section. The aim of this thesis project has been the development of a FEM-based solver for the three-dimensional (3D) problems (8) and (9). In a first phase, prototypes in one and two dimensions (1D and 2D) were written in MATLAB®. Then a major part of the project time was spent developing a 3D solver, named caaHelmholtz, in C++.

The main steps performed by the solvers are:

1. Read input data
2. Assemble FEM matrix and right hand side vector
3. Solve the linear system
4. Write results to file

The program caaHelmholtz, as well as the 1D and 2D prototypes, can handle problems on bounded domains with Dirichlet, Neumann and homogeneous Robin boundary conditions. They also include Galerkin/least-squares (GLS) stabilization. Further, caaHelmholtz can handle problems on unbounded domains, using the coupled FEM-IEM. Piecewise linear basis functions are used for the FEM in all cases; in 2D on a triangular mesh and in 3D on a tetrahedral mesh. In caaHelmholtz, linear systems of equations are solved using Intel® Math Kernel Library [25] routines.

4.1 Finite Element Spaces

In order to write a FEM formulation, such as (15), in the discrete form

$$\boldsymbol{A}\boldsymbol{u} = \boldsymbol{b},$$

a basis $\{\varphi_i\}_{i=1}^{N}$ for the FE space is needed. Letting $\{\boldsymbol{p}_j\}_{j=1}^{N}$ denote the mesh nodes, the classical choice of basis for the FE space consisting of piecewise linear functions can be written

$$\varphi_i(\boldsymbol{p}_j) = \delta_{ij}, \quad \forall i, j,$$

where the basis functions φ_i are affine on each mesh element.

In case Dirichlet conditions are prescribed at say N_{D} boundary nodes, the corresponding basis functions are excluded from the basis and the values at those nodes are in the trial functions set to the prescribed Dirichlet values and in the test functions set to zero.

4.1.1 Finite Element Shape Functions

The integrals in the FEM formulations described in Section 3.1 are computed on the element level using a mapping between mesh elements and a "master element":

- a line segment $L^\xi = [0,1]$ in 1D,
- a triangle T^ξ with corners in $(0,0), (1,0)$ and $(0,1)$ in 2D and
- a tetrahedron H^ξ with corners in $(0,0,0), (1,0,0), (0,1,0)$ and $(0,0,1)$ in 3D,

where the coordinates are given in the coordinate systems (ξ), (ξ_1, ξ_2) and (ξ_1, ξ_2, ξ_3), respectively. With $|\cdot|$ denoting length in 1D, area in 2D and volume in 3D we then have

$$\begin{aligned} |L^\xi| &= 1 \\ |T^\xi| &= \tfrac{1}{2} \\ |H^\xi| &= \tfrac{1}{6}. \end{aligned} \tag{27}$$

We will now define linear shape functions on the master elements and mappings from master elements to mesh elements. The shape functions are denoted by N_i in any dimension, as it will be clear from the context which functions are meant.

One dimensional shape functions Denote by

$$\begin{aligned} \xi^1 &= 1, \\ \xi^2 &= 0, \end{aligned}$$

the end points of L^ξ. We define linear shape functions by

$$\begin{aligned} N_1(\xi) &= \xi, \\ N_2(\xi) &= 1 - \xi. \end{aligned} \tag{28}$$

Two dimensional shape functions Denote by

$$\begin{aligned} \boldsymbol{\xi}^1 &: (1,0), \\ \boldsymbol{\xi}^2 &: (0,1), \\ \boldsymbol{\xi}^3 &: (0,0), \end{aligned}$$

the corner nodes of T^ξ. We define linear shape functions by

$$\begin{aligned} N_1(\xi_1, \xi_2) &= \xi_1, \\ N_2(\xi_1, \xi_2) &= \xi_2, \\ N_3(\xi_1, \xi_2) &= 1 - \xi_1 - \xi_2. \end{aligned} \tag{29}$$

Three dimensional shape functions Denote by

$$\begin{aligned}\boldsymbol{\xi}^1 &: (1,0,0),\\ \boldsymbol{\xi}^2 &: (0,1,0),\\ \boldsymbol{\xi}^3 &: (0,0,1),\\ \boldsymbol{\xi}^4 &: (0,0,0),\end{aligned}$$

the corner nodes of H^ξ. We define linear shape functions by

$$\begin{aligned}N_1(\xi_1,\xi_2,\xi_3) &= \xi_1,\\ N_2(\xi_1,\xi_2,\xi_3) &= \xi_2,\\ N_3(\xi_1,\xi_2,\xi_3) &= \xi_3,\\ N_4(\xi_1,\xi_2,\xi_3) &= 1-\xi_1-\xi_2-\xi_3.\end{aligned} \tag{30}$$

Note that in all the above cases we have $N_i(\boldsymbol{\xi}^j) = \delta_{ij}$. This property enables us to define in a convenient way an affine mapping Q_K from the master element to a general mesh element E_K in $\mathbb{R}^d$, with $d = 1, 2$ or 3. To this end denote the corner nodes of E_K by $\boldsymbol{x}^0, \ldots, \boldsymbol{x}^d$. We can then define

$$Q_K(\boldsymbol{\xi}) := \sum_{i=1}^{d+1} N_i(\boldsymbol{\xi})\boldsymbol{x}^{i'}, \quad i' = i \mod (d+1), \tag{31}$$

mapping node i of the master element to node i' of the mesh element[2]. The mappings are affine and can be written on matrix form in one dimension as

$$x = Q_K(\xi) = \underbrace{(x^1 - x^0)}_{=:J^K_{1D}}\xi + x^0,$$

in two dimensions as

$$\begin{pmatrix} x\\ y\end{pmatrix} = Q_K\begin{pmatrix}\xi_1\\ \xi_2\end{pmatrix} = \underbrace{\begin{pmatrix} x^1-x^0 & x^2-x^0\\ y^1-y^0 & y^2-y^0\end{pmatrix}}_{=:J^K_{2D}}\begin{pmatrix}\xi_1\\ \xi_2\end{pmatrix} + \begin{pmatrix}x^0\\ y^0\end{pmatrix},$$

and in three dimensions as

$$\begin{pmatrix} x\\ y\\ z\end{pmatrix} = Q_K\begin{pmatrix}\xi_1\\ \xi_2\\ \xi_3\end{pmatrix} = \underbrace{\begin{pmatrix} x^1-x^0 & x^2-x^0 & x^3-x^0\\ y^1-y^0 & y^2-y^0 & y^3-y^0\\ z^1-z^0 & z^2-z^0 & z^3-z^0\end{pmatrix}}_{=:J^K_{3D}}\begin{pmatrix}\xi_1\\ \xi_2\\ \xi_3\end{pmatrix} + \begin{pmatrix}x^0\\ y^0\\ z^0\end{pmatrix}.$$

---

[2] The construction with modulus, mapping the last node of the master element to the zeroth node of the mesh element assures that the determinant of the Jacobian of Q_K is positive if the corner nodes $\boldsymbol{x}^0, \ldots, \boldsymbol{x}^d$ are numbered according to a standard convention.

With this formulation it is clear that J_{1D}^K, J_{2D}^K and J_{3D}^K are the Jacobians of the mapping Q_K in one, two and three dimensions respectively. We further note that the inverse of Q_K exists whenever the determinant of the Jacobian is nonzero which geometrically corresponds to the mesh element E_K having nonzero length (in one dimension), area (in two dimensions) or volume (in three dimensions). This is a reasonable property to expect from our mesh elements and we will hence assume, in general, that Q_K^{-1} exists.

Having shape functions N_i on the master element and the invertible mapping Q_K from the master element to a mesh element E_K we can define linear shape functions N_i^K on E_K:

$$N_{i'}^K(\boldsymbol{x}) := N_i(Q_K^{-1}(\boldsymbol{x})), \quad i' = i \mod (d+1). \tag{32}$$

The local shape functions N_i^K inherit the following property from the shape functions N_i:

$$N_i^K(\boldsymbol{x}^j) = \delta_{ij}, \quad i,j = 0,\dots,d.$$

4.1.2 An Alternative Mapping Formulation

An alternative way of defining the mappings is by using barycentric coordinates. We introduce an auxiliary variable

$$\begin{array}{ll} \xi_2 := 1 - \xi_1 & \text{in one dimension (with } \xi_1 := \xi\text{),} \\ \xi_3 := 1 - \xi_1 - \xi_2 & \text{in two dimensions and} \\ \xi_4 := 1 - \xi_1 - \xi_2 - \xi_3 & \text{in three dimensions.} \end{array}$$

Any shape function, as defined in (28), (29) or (30), can then be written as

$$\tilde{N}_i(\boldsymbol{\xi}) = \xi_i,$$

where the ˜ sign indicates that the argument $\boldsymbol{\xi}$ has dimension $d+1$, rather than d as previously. With barycentric coordinates, the shape functions are thus equal to the coordinates.

The mapping from master element to mesh element can now be defined as in (31) with the additional requirement $\sum_{i=1}^{d+1} \xi_i = 1$. In matrix form we then have in one dimension

$$\begin{pmatrix} x \\ 1 \end{pmatrix} = \tilde{Q}_K \begin{pmatrix} \xi_1 \\ \xi_2 \end{pmatrix} = \underbrace{\begin{pmatrix} x^1 & x^0 \\ 1 & 1 \end{pmatrix}}_{=:J_{1D}^{K,2\times 2}} \begin{pmatrix} \xi_1 \\ \xi_2 \end{pmatrix},$$

in two dimensions

$$\begin{pmatrix} x \\ y \\ 1 \end{pmatrix} = \tilde{Q}_K \begin{pmatrix} \xi_1 \\ \xi_2 \\ \xi_3 \end{pmatrix} = \underbrace{\begin{pmatrix} x^1 & x^2 & x^0 \\ y^1 & y^2 & y^0 \\ 1 & 1 & 1 \end{pmatrix}}_{=:J_{2D}^{K,3\times 3}} \begin{pmatrix} \xi_1 \\ \xi_2 \\ \xi_3 \end{pmatrix},$$

and in three dimensions

$$\begin{pmatrix} x \\ y \\ z \\ 1 \end{pmatrix} = \tilde{Q}_K \begin{pmatrix} \xi_1 \\ \xi_2 \\ \xi_3 \\ \xi_4 \end{pmatrix} = \underbrace{\begin{pmatrix} x^1 & x^2 & x^3 & x^0 \\ y^1 & y^2 & y^3 & y^0 \\ z^1 & z^2 & z^3 & z^0 \\ 1 & 1 & 1 & 1 \end{pmatrix}}_{=:J_{3D}^{K,4\times 4}} \begin{pmatrix} \xi_1 \\ \xi_2 \\ \xi_3 \\ \xi_4 \end{pmatrix},$$

where $J_{1D}^{K,2\times 2}$, $J_{2D}^{K,3\times 3}$ and $J_{3D}^{K,4\times 4}$ are the corresponding Jacobian matrices.

It can be verified that, as expected,

$$\begin{aligned} \det(J_{1D}^{K,2\times 2}) &= \det(J_{1D}^{K}), \\ \det(J_{2D}^{K,3\times 3}) &= \det(J_{2D}^{K}), \\ \det(J_{3D}^{K,4\times 4}) &= \det(J_{3D}^{K}). \end{aligned}$$

The linear shape functions N_i^K on E_K, defined in (32), can then be written as

$$N_{i'}^K(\boldsymbol{x}) = \tilde{N}_i(\tilde{Q}_K^{-1}(\boldsymbol{x})), \quad i' = i \mod (d+1).$$

Note that this is not a redefinition of N_i^K, but merely an alternative formulation of the same functions.

4.2 Evaluation of Integrals

Using the shape functions and mappings defined above we will now evaluate the integrals appearing in the FEM and IEM-FEM formulations in Section 3.

4.2.1 Integrals over Finite Elements

Throughout this section we will assume

$$i' = i \mod (d+1), \quad i = 1, \ldots, d+1,$$

and the corresponding relation between j' and j.

Mass Matrix For the assembly of the mass matrix $\boldsymbol{M}$ (see Section 3.1.1) integrals of type

$$M_{i'j'}^K = \int_{E_K} N_{i'}^K(\boldsymbol{x}) N_{j'}^K(\boldsymbol{x}) \,\mathrm{d}\boldsymbol{x} \tag{33}$$

need to be computed. Using the mapping $\tilde{Q}_K$, and denoting by E^ξ the master element in d dimensions, we have

$$\begin{aligned} M^K_{i'j'} &= \int_{E^\xi} N^K_{i'}(\tilde{Q}_K(\boldsymbol{\xi}))N^K_{j'}(\tilde{Q}_K(\boldsymbol{\xi}))\det(J^K)\,\mathrm{d}\boldsymbol{\xi} \\ &= \int_{E^\xi} \tilde{N}_i(\boldsymbol{\xi})\tilde{N}_j(\boldsymbol{\xi})\det(J^K)\,\mathrm{d}\boldsymbol{\xi} \\ &= \int_{E^\xi} \xi_i\xi_j \det(J^K)\,\mathrm{d}\boldsymbol{\xi}, \end{aligned}$$

where J^K is the Jacobian matrix of $\tilde{Q}_K$. Since $\tilde{Q}_K$ is linear, J^K is independent of $\boldsymbol{\xi}$, and we get

$$M^K_{i'j'} = \det(J^K)\cdot M^\xi_{ij}, \tag{34}$$

with

$$M^\xi_{ij} = \int_{E^\xi} \xi_i\xi_j\,\mathrm{d}\boldsymbol{\xi},$$

or explicitly in one dimension

$$\boldsymbol{M}^\xi = \frac{1}{6}\begin{pmatrix} 2 & 1 \\ 1 & 2 \end{pmatrix},$$

in two dimensions

$$\boldsymbol{M}^\xi = \frac{1}{24}\begin{pmatrix} 2 & 1 & 1 \\ 1 & 2 & 1 \\ 1 & 1 & 2 \end{pmatrix},$$

and in three dimensions

$$\boldsymbol{M}^\xi = \frac{1}{120}\begin{pmatrix} 2 & 1 & 1 & 1 \\ 1 & 2 & 1 & 1 \\ 1 & 1 & 2 & 1 \\ 1 & 1 & 1 & 2 \end{pmatrix}.$$

Stiffness Matrix To assemble the stiffness matrix $\boldsymbol{K}$ (see Section 3.1.1) we need to evaluate integrals of type

$$K^K_{i'j'} = \int_{E_K} (\nabla_x N^K_{i'}(\boldsymbol{x}))^T(\nabla_x N^K_{j'}(\boldsymbol{x}))\,\mathrm{d}\boldsymbol{x}.$$

Using again the mapping $\tilde{Q}_K$ we note that ∇_x (of length d) is related to ∇_ξ (of length $d+1$) through

$$\nabla_x = \underbrace{\begin{pmatrix} \frac{\partial\xi_1}{\partial x_1} & \cdots & \frac{\partial\xi_{d+1}}{\partial x_1} \\ \vdots & \ddots & \vdots \\ \frac{\partial\xi_1}{\partial x_d} & \cdots & \frac{\partial\xi_{d+1}}{\partial x_d} \end{pmatrix}}_{=:D^K} \nabla_\xi,$$

where the matrix D^K equals the first d rows of the transposed inverse of J^K. With this notation we have

$$\begin{aligned} K^K_{i'j'} &= \int_{E^\xi} (D^K \cdot \nabla_\xi N^K_{i'}(\tilde{Q}_K(\boldsymbol{\xi})))^T (D^K \cdot \nabla_\xi N^K_{j'}(\tilde{Q}_K(\boldsymbol{\xi}))) \det(J^K)\,\mathrm{d}\boldsymbol{\xi} \\ &= \int_{E^\xi} (D^K \cdot \nabla_\xi \tilde{N}_i(\boldsymbol{\xi}))^T (D^K \cdot \nabla_\xi \tilde{N}_j(\boldsymbol{\xi})) \det(J^K)\,\mathrm{d}\boldsymbol{\xi}. \end{aligned}$$

Now, since $\tilde{N}_i(\boldsymbol{\xi}) = \xi_i$, $\nabla_\xi \tilde{N}_i(\boldsymbol{\xi})$ is the i$^{\text{th}}$ unit vector and the integrand simplifies to

$$((D^K)^T \cdot D^K)_{ij} \det(J^K),$$

an expression independent of $\boldsymbol{\xi}$, and we write

$$\begin{aligned} K^K_{i'j'} &= ((D^K)^T \cdot D^K)_{ij} \det(J^K) \int_{E^\xi} \mathrm{d}\boldsymbol{\xi} \\ &= |E^\xi|((D^K)^T \cdot D^K)_{ij} \det(J^K), \end{aligned}$$

where the value of $|E^\xi|$ is given by (27) for $d = 1, 2, 3$.

Right Hand Side For the Helmholtz equation (8), assuming f to be given numerically as having a constant value f^K on each mesh element E_K, integrals of type

$$b^K_{i'} = f^K \int_{E_K} N^K_{i'}(\boldsymbol{x})\,\mathrm{d}\boldsymbol{x} \tag{35}$$

need to be computed, and we find, using again integration by substitution,

$$b^K_{i'} = f^K \det(J^K) b^\xi_i, \tag{36}$$

where in one dimension

$$b^\xi_i = \frac{1}{2}, \quad i = 1, 2,$$

in two dimensions

$$b^\xi_i = \frac{1}{6}, \quad i = 1, 2, 3,$$

and in three dimensions

$$b^\xi_i = \frac{1}{24}, \quad i = 1, 2, 3, 4,$$

and J^K is the Jacobian of Q_K.

If f is given as nodal values we interpolate linearly between nodes and compute

$$b^K_{i'} = \sum_{j'} f^K_{j'} \int_{E_K} N^K_{i'}(\boldsymbol{x}) N^K_{j'}(\boldsymbol{x})\,\mathrm{d}\boldsymbol{x} = \boldsymbol{M}^K \boldsymbol{f}^K,$$

where the entries of matrix M^K are defined as in (33) and the entries $f^K_{j'}$ of vector $\boldsymbol{f}$ are the nodal values (with local numbering on element E_K) of f.

Neumann and Robin Boundary Conditions To impose boundary conditions, integration over boundary elements B_K must be performed. In a three-dimensional mesh we consider triangular boundary elements and in a two-dimensional mesh line segments. In one dimension, boundary elements reduce to points and no integration is needed.

We assume the boundary conditions are given as

$$\begin{aligned} \frac{\partial u}{\partial n} &= g \quad \text{on } B_K \quad \text{(Neumann), or} \\ \alpha u + \frac{\partial u}{\partial n} &= 0 \quad \text{on } B_K \quad \text{(homogeneous Robin),} \end{aligned}$$

where g or α is constant over B_K. For Neumann and Robin conditions we then need to compute integrals of type (35) and (33), respectively, with integration over B_K rather than over E_K. The mapping Q defined in (31) can still be used, but now its Jacobian is not a square matrix, so rather than the determinant of the Jacobian we use

$$\frac{|B_K|}{|B^\xi|},$$

where B^ξ is the master element corresponding to B_K. With this substitution, the expressions (34) and (36) still hold for the evaluation of the desired integrals.

4.2.2 Integrals over Infinite Elements

We now come to the evaluation of integrals appearing in the infinite element formulation, i.e., the expression in (26). Integration over the FE domain Ω_{r_0} is performed as previously discussed for the FE case.

Let us introduce the additional notation

$$a^+(u, v) = \int_{\Omega^+_{r_0}} (\nabla u \cdot \nabla \bar{v} - k^2 u \bar{v})\, \mathrm{d}V, \tag{37}$$

for the IE part of the sesquilinear form (26). We will compute the integral in (37) for a pair of IE trial and test basis functions

$$\begin{aligned} u_{\alpha,\beta} &= U_\beta(r) u^h_\alpha(\boldsymbol{s}), \quad 1 \le \beta \le N_\mathrm{r}, \\ v_{\mu,\nu} &= V_\nu(r) v^h_\mu(\boldsymbol{s}), \quad 3 \le \nu \le N_\mathrm{r} + 2. \end{aligned}$$

Expanding the integral in coordinates $(r, \boldsymbol{s})$, we have

$$a^+(u, v) = \int_{r_0}^{\infty} r^2 \int_{S_0} (\nabla u \cdot \nabla \bar{v} - k^2 u \bar{v})\, \mathrm{d}S\, \mathrm{d}r,$$

where S_0 is the unit sphere. The gradient in these coordinates takes the form

$$\nabla = \frac{\partial}{\partial r}\mathbf{e}_r + \frac{1}{r}\nabla_S,$$

where ∇_S is the gradient with respect to $\boldsymbol{s}$, and we have, when separating variables,

$$\begin{aligned} a^+(u_{\alpha,\beta}, v_{\mu,\nu}) = &\int_{r_0}^{\infty} r^2 \left(\frac{\partial U_\beta}{\partial r}\frac{\partial \overline{V_\nu}}{\partial r} - k^2 U_\beta \overline{V_\nu} \right) \mathrm{d}r \int_{S_0} u_\alpha^h \bar{v}_\mu^h \,\mathrm{d}S \\ &+ \int_{r_0}^{\infty} U_\beta \overline{V_\nu}\,\mathrm{d}r \int_{S_0} \nabla_S u_\alpha^h \cdot \nabla_S \bar{v}_\mu^h \,\mathrm{d}S. \end{aligned}$$

We thus need to compute the following integrals:

$$\begin{aligned} A_{\nu,\beta} &= \int_{r_0}^{\infty} U_\beta \overline{V_\nu}\,\mathrm{d}r, \\ B_{\nu,\beta} &= \int_{r_0}^{\infty} r^2 U_\beta \overline{V_\nu}\,\mathrm{d}r, \\ C_{\nu,\beta} &= \int_{r_0}^{\infty} r^2 \frac{\partial U_\beta}{\partial r}\frac{\partial \overline{V_\nu}}{\partial r}\,\mathrm{d}r, \\ D_{\mu,\alpha} &= \int_{S_0} u_\alpha^h \bar{v}_\mu^h \,\mathrm{d}S, \\ E_{\mu,\alpha} &= \int_{S_0} \nabla_S u_\alpha^h \cdot \nabla_S \bar{v}_\mu^h \,\mathrm{d}S, \end{aligned}$$

and can then evaluate

$$a^+(u_{\alpha,\beta}, v_{\mu,\nu}) = (C_{\nu,\beta} - k^2 B_{\nu,\beta}) D_{\mu,\alpha} + A_{\nu,\beta} E_{\mu,\alpha}. \tag{38}$$

Due to the conjugated formulation, evaluation of integrals $A_{\nu,\beta}$ and $B_{\nu,\beta}$ is trivial:

$$A_{\nu,\beta} = \frac{r_0}{\nu + \beta - 1}, \tag{39}$$

$$B_{\nu,\beta} = \frac{r_0^3}{\nu + \beta - 3}. \tag{40}$$

Note that both integrals are convergent, since $\beta \geq 1$ and $\nu \geq 3$. This is a sufficient condition also for $C_{\nu,\beta}$ to converge.

For $C_{\nu,\beta}$ we compute derivatives with respect to r

$$\begin{aligned} \frac{\partial U_\beta(r)}{\partial r} &= U_\beta(r)(ik - \frac{\beta}{r}), \\ \frac{\partial \overline{V_\nu}(r)}{\partial r} &= \overline{V_\nu}(r)(-ik - \frac{\nu}{r}), \end{aligned}$$

and find

$$C_{\nu,\beta} = \left(\frac{r_0^3 k^2}{\beta+\nu-3} + \frac{r_0^2 ik(\beta-\nu)}{\beta+\nu-2} + \frac{r_0\beta\nu}{\beta+\nu-1} \right). \tag{41}$$

Inserting (39), (40) and (41) into (38) yields

$$a^+(u_{\alpha,\beta}, v_{\mu,\nu}) = \left(\frac{r_0^2 ik(\beta-\nu)}{\beta+\nu-2} + \frac{r_0\beta\nu}{\beta+\nu-1} \right) D_{\mu,\alpha} + \frac{r_0}{\nu+\beta-1} E_{\mu,\alpha}. \tag{42}$$

It remains the evaluation of $D_{\mu,\alpha}$ and $E_{\mu,\alpha}$. As was previously mentioned, the angular basis functions $u_{\mu,\alpha}$ and $v_{\mu,\alpha}$ should be chosen such that they match the FE basis functions on Γ_{r_0}. Since Γ_{r_0} is discretized by piecewise linear elements (triangles, in the three dimensional case), approximating the spherical surface, the integrals over S_0 will be approximated by a sum of integrals over such triangular elements.

For the evaluation of $D_{\mu,\alpha}$ we can readily use the results obtained in Section 4.2.1 for Robin boundary conditions, only scaling the integrals by $(1/r_0^2)$ to compensate for the fact that integration is performed over Γ_{r_0} with radius r_0, rather than over S_0, the surface of the unit sphere. For $E_{\mu,\alpha}$, however, we need a local approximation of ∇_S on each boundary element (i.e., triangle) $T_K \subset \Gamma_{r_0}$. To that end we introduce a local orthogonal coordinate system (η_1, η_2) lying in the plane of T_K. Denote the corners of T_K by $\boldsymbol{x}^0, \boldsymbol{x}^1, \boldsymbol{x}^2$, as in Section 4.1.1, and define

$$\begin{aligned} \boldsymbol{v}_1 &= \boldsymbol{x}^1 - \boldsymbol{x}^0, \\ \boldsymbol{v}_2 &= \boldsymbol{x}^2 - \boldsymbol{x}^0. \end{aligned}$$

We then let the direction of the η_1 axis be that of $\boldsymbol{v}_1$ and the direction of the η_2 axis be that of $[\boldsymbol{v}_1 \times \boldsymbol{v}_2] \times \boldsymbol{v}_1$ and define a mapping Φ from (η_1, η_2) to global Cartesian coordinates (x, y, z) through

$$\Phi(\eta_1, \eta_2) = \eta_1 \frac{1}{l_1} \boldsymbol{v}_1 + \eta_2 \frac{1}{l_3} \left(\boldsymbol{v}_2 - \frac{l_2}{l_3} \boldsymbol{v}_1 \right) + \boldsymbol{x}^0,$$

with

$$\begin{aligned} l_1 &= \|\boldsymbol{v}_1\|, \\ l_2 &= \frac{1}{l_1} \boldsymbol{v}_1 \cdot \boldsymbol{v}_2, \\ l_3 &= \|\boldsymbol{v}_2 - \frac{l_2}{l_1} \boldsymbol{v}_1\|. \end{aligned}$$

Now, denoting by $T_K^\eta$the triangle with corners in $\boldsymbol{\eta}^0 : (0,0)$, $\boldsymbol{\eta}^1 : (l_1, 0)$ and $\boldsymbol{\eta}^2 : (l_2, l_3)$ it can be seen that Φ maps T_K^η onto T_K with no distortion nor rescaling. More specifically we have

$$\Phi(\boldsymbol{\eta}^i) = \boldsymbol{x}^i, \qquad i = 0, 1, 2.$$

We can now approximate ∇_S locally on T_K by $\nabla_\eta = (\frac{\partial}{\partial\eta_1}, \frac{\partial}{\partial\eta_2})$ and write

$$\begin{aligned} E_{\mu,\alpha} &= \int_{S_0} \nabla_S u_\alpha^h \cdot \nabla_S \bar{v}_\mu^h \,\mathrm{d}S = \int_{\Gamma_{r_0}} \frac{1}{r_0^2}(r_0 \nabla_S u_\alpha^h)\cdot(r_0\nabla_S \bar{v}_\mu^h)\,\mathrm{d}S \\ &= \int_{\Gamma_{r_0}} \nabla_S u_\alpha^h \cdot \nabla_S \bar{v}_\mu^h \,\mathrm{d}S \approx \sum_K \int_{T_K^\eta} \nabla_\eta u_\alpha^h \cdot \nabla_\eta \bar{v}_\mu^h \,\mathrm{d}\boldsymbol{\eta}. \end{aligned}$$

The global basis functions u_α^h and v_μ^h are constructed in the usual way using local shape functions on boundary elements adjacent to the nodes with global node numbers α and μ, respectively. The integrals are evaluated as described in Section 4.2.1 for the stiffness matrix in two dimensions, with the modification that Q_K maps E^ξ to T_K^η rather than to T_K. Note that the Jacobian matrix of $\tilde{Q}_K$ then takes the form

$$J_{2D}^K = \begin{pmatrix} l_1 & l_2 & 0 \\ 0 & l_3 & 0 \\ 1 & 1 & 1 \end{pmatrix},$$

with determinant $l_1 l_3$, which is as expected twice the area of T_K, i.e.,

$$\det(J_{2D}^K) = \frac{|T_K|}{|E^\xi|}.$$

As in Section 4.2.1, we have

$$\nabla_\eta = D^K \nabla_\xi,$$

where the matrix D^K is the first two rows of $(J_{2D}^K)^{-T}$, which in this case takes the form

$$D^K = \frac{1}{l_1 l_3}\begin{pmatrix} l_3 & 0 & -l_3 \\ -l_2 & l_1 & l_2 - l_1 \end{pmatrix}.$$

Substituting the global indices μ and α for local indices i', j' on the boundary element T_K we have

$$\begin{aligned} E_{i',j'} &= \int_{T_K^\eta} (\nabla_\eta N_{i'}^K(\boldsymbol{\eta}))^T (\nabla_\eta N_{j'}^K(\boldsymbol{\eta}))\,\mathrm{d}\boldsymbol{\eta} \\ &= \int_{E^\xi} (D^K \nabla_\xi N_{i'}^K(\tilde{Q}_K(\boldsymbol{\xi})))^T (D^K \nabla_\xi N_{j'}^K(\tilde{Q}_K(\boldsymbol{\xi})))\det(J_{2D}^K)\,\mathrm{d}\boldsymbol{\xi} \\ &= \int_{E^\xi} (D^K \nabla_\xi \tilde{N}_i(\boldsymbol{\xi}))^T (D^K \nabla_\xi \tilde{N}_j(\boldsymbol{\xi}))\det(J_{2D}^K)\,\mathrm{d}\boldsymbol{\xi}, \end{aligned}$$

with the usual convention, that $i' = i \mod 2, i = 1,2,3$. We use as before that $\nabla_\xi \tilde{N}_i(\boldsymbol{\xi})$ is the i$^{\text{th}}$ unit vector, to see that

$$E_{i',j'} = ((D^K)^T D^K)_{ij}\det(J_{2D}^K)\int_{E^\xi}\mathrm{d}\boldsymbol{\xi} = ((D^K)^T D^K)_{ij}|T_K|.$$

4.3 Matrix and Right Hand Side Vector Assembly

The full matrix $\boldsymbol{A}$ and right hand side vector $\boldsymbol{b}$ are assembled by computing the integrals on individual mesh elements as described in the previous sections and adding the contributions to the corresponding matrix and vector elements, letting, as previously described, each mesh node correspond to one basis function. In the case of IEM of radial order N_r, each node coupled to an infinite element corresponds to N_r basis functions, each with a different polynomial order in the radial direction. With a good node numbering this leads to a blocked, banded matrix structure as can be seen in Figure 4.1

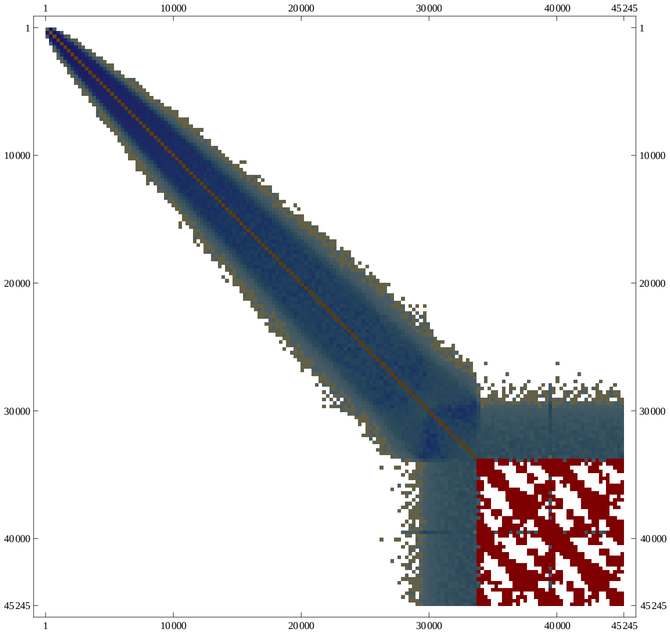

Figure 4.1: Structure of assembled matrix. The blocked structure in the lower right part of the matrix results from IE of second radial order. Red color indicates matrix elements with non-zero imaginary part.

4.4 Handling Complex Data

With real-valued basis functions in the FE domain, e.g. as described in Section 4.1, the mass and stiffness matrices are always real. We also assume that the wave number k is real, hence the FEM matrix $\boldsymbol{K} - k^2\boldsymbol{M}$ is real. The linear system to be solved, i.e.,

$$\boldsymbol{A}\boldsymbol{u} = \boldsymbol{b}, \tag{43}$$

can be complex in two distinct senses:

1. The right hand side vector $\boldsymbol{b}$ can be complex, due to complex sources or complex boundary values of Dirichlet or Neumann type, while the matrix $\boldsymbol{A}$ being real.

2. The matrix $\boldsymbol{A}$ can be complex, due to complex boundary values of Robin type or if infinite elements are used (recall that the radial basis functions are complex-valued, and that the sesquilinear form in (25) evaluates on the IE domain to the complex expression in (42)).

Let N denote the size of the linear system, i.e., the number of rows (and columns) in the square matrix $\boldsymbol{A}$. Further denote by $\boldsymbol{X}^{\mathrm{Re}}$ and $\boldsymbol{X}^{\mathrm{Im}}$ the real and imaginary part of the variable $\boldsymbol{X}$, respectively. In the first of the above cases, we have

$$\begin{cases} \mathrm{Re}(\boldsymbol{A}\boldsymbol{u}) = \boldsymbol{A}\boldsymbol{u}^{\mathrm{Re}} = \boldsymbol{b}^{\mathrm{Re}} \\ \mathrm{Im}(\boldsymbol{A}\boldsymbol{u}) = \boldsymbol{A}\boldsymbol{u}^{\mathrm{Im}} = \boldsymbol{b}^{\mathrm{Im}} \end{cases}$$

and in order to solve the system (43) we merely need to solve two (real) systems of size N, namely one for the right hand side $\boldsymbol{b}^{\mathrm{Re}}$ and one for $\boldsymbol{b}^{\mathrm{Im}}$.

In the second case we have

$$\begin{cases} \mathrm{Re}(\boldsymbol{A}\boldsymbol{u}) = \boldsymbol{A}^{\mathrm{Re}}\boldsymbol{u}^{\mathrm{Re}} - \boldsymbol{A}^{\mathrm{Im}}\boldsymbol{u}^{\mathrm{Im}} = \boldsymbol{b}^{\mathrm{Re}} \\ \mathrm{Im}(\boldsymbol{A}\boldsymbol{u}) = \boldsymbol{A}^{\mathrm{Im}}\boldsymbol{u}^{\mathrm{Re}} + \boldsymbol{A}^{\mathrm{Re}}\boldsymbol{u}^{\mathrm{Im}} = \boldsymbol{b}^{\mathrm{Im}} \end{cases}$$

or in block matrix form

$$\begin{pmatrix} \boldsymbol{A}^{\mathrm{Re}} & -\boldsymbol{A}^{\mathrm{Im}} \\ \boldsymbol{A}^{\mathrm{Im}} & \boldsymbol{A}^{\mathrm{Re}} \end{pmatrix} \begin{pmatrix} \boldsymbol{u}^{\mathrm{Re}} \\ \boldsymbol{u}^{\mathrm{Im}} \end{pmatrix} = \begin{pmatrix} \boldsymbol{b}^{\mathrm{Re}} \\ \boldsymbol{b}^{\mathrm{Im}} \end{pmatrix}.$$

Here the real and imaginary solutions are coupled, and in the current implementation the above real system of size $2N$ is solved. An alternative would be to use a linear solver handling complex data.

5 Numerical Results in 1D and 2D

In this section, preliminary results using the 1D and 2D solver prototypes are presented for a few test cases. The main feature of the results, as we shall see, is the improvement achieved by using GLS stabilization, as compared to the standard Galerkin method.

5.1 1D Prototype

Results are presented for two 1D cases of the Helmholtz equation (8) with different boundary conditions and right hand sides. The standard Galerkin solution is compared to the stabilized GLS solution on a coarse mesh on which the need for stabilization is clearly visible.

Case 1: Dirichlet boundary conditions at $x = 0$ and $x = 1$;

$$u(0) = 5,$$
$$u(1) = 0,$$

and $f(x) = \cos(kx)$. Results are shown in Figure 5.1 for the case that $k = 10$ and using a uniform mesh with mesh size $h = 0.1$. The standard Galerkin solution has correct phase but a large error in amplitude, whereas the GLS solution displays good accuracy in phase as well as amplitude and is nodally exact. On a finer mesh both methods perform well.

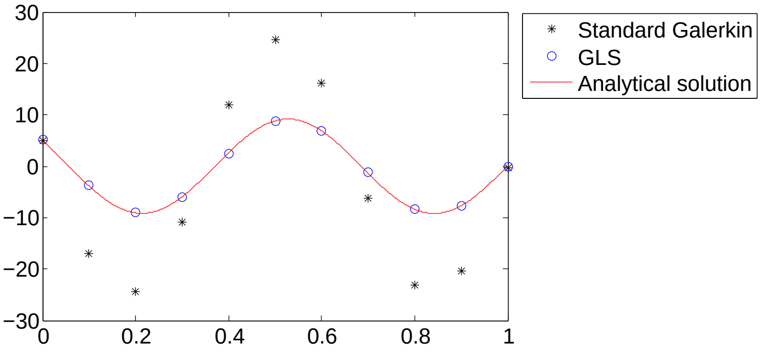

Figure 5.1: Real part of the solution to 1D test Case 1.

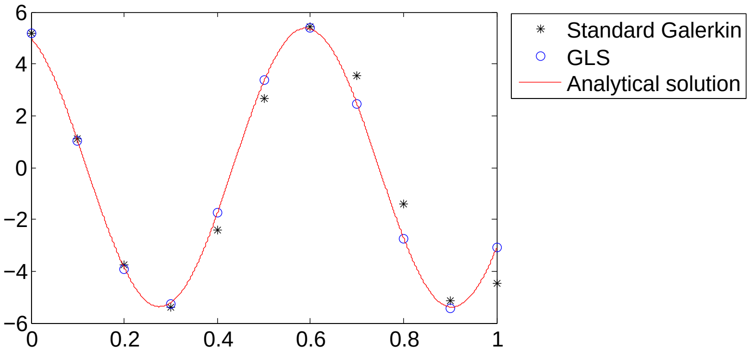

Figure 5.2: Real part of the solution to 1D test Case 2.

Case 2: Dirichlet boundary condition at $x = 0$ and Robin boundary condition (corresponding to Sommerfeld's radiation condition in 1D, see [24]) at $x = 1$;

$$u(0) = 5,$$
$$u'(1) = iku(1),$$

and $f(x) = 0$. In Figure 5.2, the results for $k = 10$, using the same mesh as in Case 1, are displayed. Again, the GLS solution is nodally exact, except at $x = 0$, i.e., at the weakly imposed Dirichlet boundary condition, while the standard Galerkin solution has an error - however much smaller than in Case 1 - in amplitude.

5.2 2D Prototype

A two-dimensional test case is taken from [30], Section 6.3. The Helmholtz equation was solved for $k = 8$ on the square $[0, 1] \times [0, 1]$ with homogeneous Dirichlet boundary conditions at the entire boundary and with the source term $f(x, y) = \delta(x - x_0)(y - y_0)$, where $(x_0, y_0) = (0.1875, 0.1875)$. In Figure 5.3 the GLS solution and the (truncated) analytical solution on the entire domain are shown. The analytical solution along the line $y = 0.2$ is shown in Figure 5.4 along with the standard Galerkin and GLS solutions. Away from the singularity in (x_0, y_0), the behavior of the analytical solution is captured well by the GLS solution while, as in the 1D case, the standard Galerkin solution has a clearly visible error.

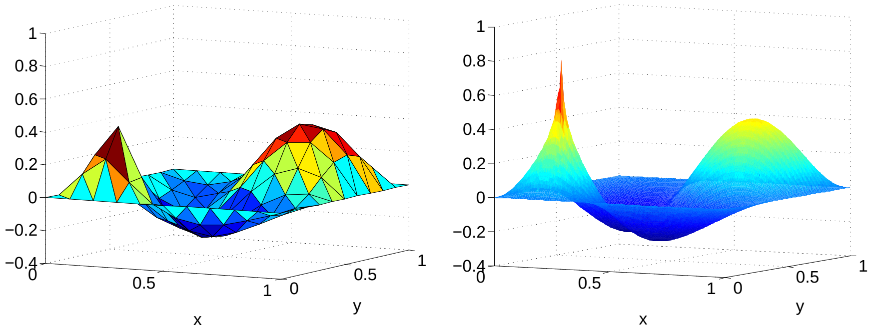

(a) GLS solution. **(b)** Truncated analytical solution.

Figure 5.3: 2D test case.

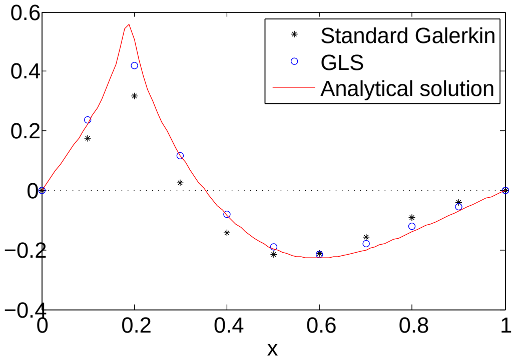

Figure 5.4: 2D test case. Solution at $y = 0.2$.

6 Numerical Results in 3D Using caaHelmholtz

For all 3D cases, meshes were generated using Gmsh© [17].

6.1 Plane Wave in Box

We first consider the homogeneous Helmholtz equation in a box:

$$\begin{array}{ll} -\Delta u - k^2 u = 0 & \text{in } I_x \times I_y \times I_z, \\ \frac{\partial u}{\partial n} = 0 & \text{on } \Gamma_{\mathrm{N}}, \\ u = 0 & \text{on } \Gamma_{\mathrm{D}_0}, \\ u = \sin(k l_z) & \text{on } \Gamma_{\mathrm{D}_1}, \end{array} \tag{44}$$

where $I_x = [0, l_x]$, $I_y = [0, l_y]$ and $I_z = [0, l_z]$ and

$$\begin{aligned} \Gamma_{\mathrm{N}} &= (\{0, l_x\} \times I_y \times I_z) \cup (I_x \times \{0, l_y\} \times I_z), \\ \Gamma_{\mathrm{D}_0} &= I_x \times I_y \times \{0\}, \\ \Gamma_{\mathrm{D}_1} &= I_x \times I_y \times \{l_z\}. \end{aligned}$$

The homogeneous Neumann conditions on four sides together with constant Dirichlet conditions at the two remaining (opposite) sides leads to a plane wave along the z direction. The Dirichlet conditions are chosen such that the analytical solution is real valued and takes the simple form:

$$u(x, y, z) = \sin(kz)$$

for $k \neq \frac{n\pi}{l_z}$, with $n \in \mathbb{Z}$.

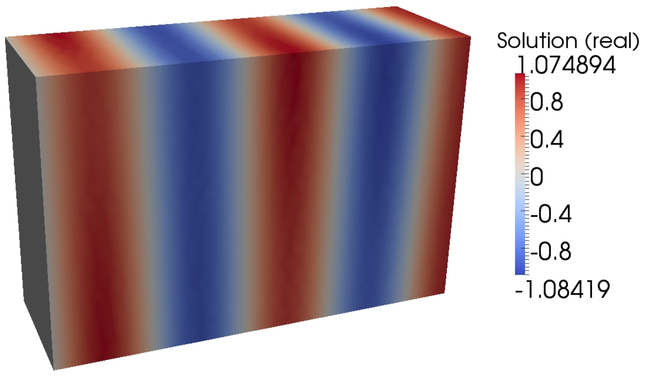

Figure 6.1: Numerical solution in box for $k = 4.7$ with mesh size $h = 0.1$.

The above problem was solved using caaHelmholtz for a box of size $l_x = 1$, $l_y = 2$, $l_z = 3$ with meshes of varying mesh size h. The numerical solution at the box surface is shown in Figure 6.1 for $k = 4.7$ and $h = 0.1$. In Figure 6.2, the numerical solution for the same case is shown together with the analytical solution along the central axis of the box in the z direction. The numerical solution is nearly indistinguishable from the analytical one, except at the maximum and minimum points, where the amplitude is somewhat underestimated.

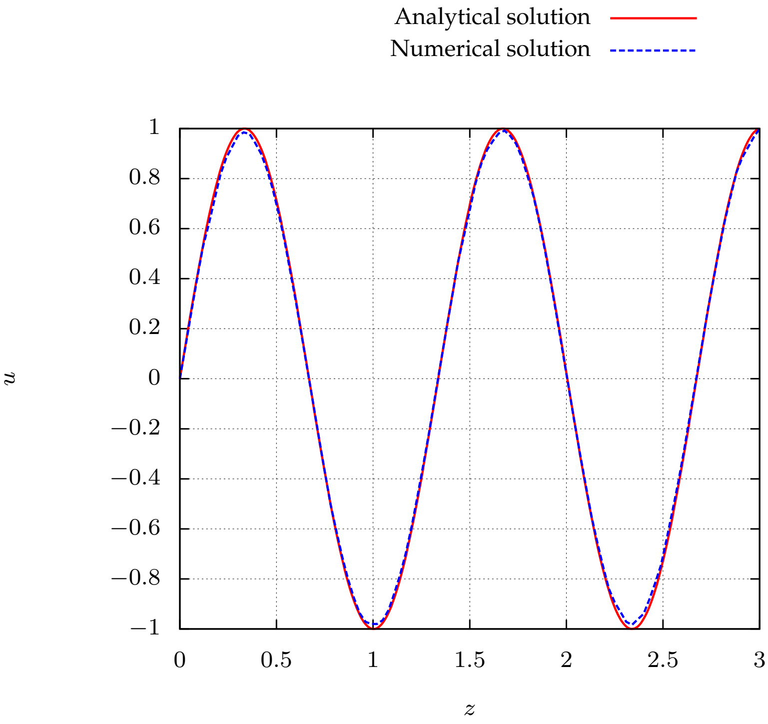

Figure 6.2: Solution along line in z direction for $k = 4.7$ with mesh size $h = 0.1$.

Maximal nodal errors of the solutions to problem (44) with $k = 4.7$ using three meshes with different refinements are listed in Table 6.1. We note that the error decreases as the mesh size is reduced, indicating that the numerical solution converges to the exact one when the mesh is refined. To make a real convergence analysis a framework for computing integral norms of the error would be needed.

Table 6.1: Maximal nodal errors for $k = 4.7$.

Mesh size (h)	0.035	0.1	0.25
Error	0.075	0.12	0.36

6.2 Resonance in a Flanged Pipe Closed at one End

In the previous case, the domain was bounded. We now come to the first 3D case on an unbounded domain.

Resonance frequencies Consider a pipe closed at one end and flanged at the other. In such a pipe, of length L and radius r_p, resonance occurs approximately at frequencies corresponding to wave numbers $k = k_m$ solving

$$x \tan^2 kL + (r^2 + x^2 - 1)\tan kL - x = 0, \tag{45}$$

where

$$\begin{aligned} r &= \frac{(2kr_p)^2}{2\cdot 4} - \frac{(2kr_p)^4}{2\cdot 4^2\cdot 6} + \frac{(2kr_p)^6}{2\cdot 4^2\cdot 6^2\cdot 8} - \dots, \\ x &= \frac{4}{\pi}\left(\frac{2kr_p}{3} - \frac{(2kr_p)^3}{3^2\cdot 5} + \frac{(2kr_p)^5}{3^2\cdot 5^2\cdot 7} - \dots\right), \end{aligned}$$

see [26]. For low frequencies, with $kr_p \ll 1$, the resonance frequencies resulting from (45) can be approximated by

$$f_m^{\text{approx}} = \frac{2m-1}{4}\frac{a_0}{L + (8/3\pi)r_p}, \qquad m = 1, 2, \dots, \tag{46}$$

corresponding to resonance at wave lengths

$$\lambda_m^{\text{approx}} = \frac{4}{2m-1}L_{\text{eff}},$$

where $L_{\text{eff}} = L + (8/3\pi)r_p$ is the (approximate) effective length of the pipe.

The first few resonance frequencies, computed approximately by (46) as well as more accurately by (45), for a pipe of length $L = 1\text{m}$ and radius $r_p = 0.05\text{m}$ are listed in Table 6.2. The difference may seem negligible, and in the literature, often only the approximate formula is mentioned, but as we will see, relative to the numerical error, this approximation error is not negligible, and we will therefore use the frequencies computed from (45).

Table 6.2: First four resonance frequencies and corresponding wave numbers in a flanged pipe, closed at one end, with length $L = 1\text{m}$ and radius $r_p = 0.05\text{m}$.

m	f_m	k_m	f_m^{approx}	k_m^{approx}
1	82.36	1.507	82.35	1.507
2	247.31	4.525	247.06	4.521
3	412.82	7.553	411.77	7.534
4	579.05	10.595	576.48	10.548

As the resonance frequencies can be determined theoretically (or experimentally), the correctness of the numerical solution can be assessed by comparing the frequency at which resonance occurs in the numerical solution to the expected frequencies of resonance.

Test set-up Simulations were performed with a pipe of length $1\mathrm{m}$ and radius $0.05\mathrm{m}$. At the open end the FE domain was truncated with a hemisphere, centered at the pipe opening, at which the finite elements were coupled to a layer of infinite elements. At all other parts of the boundary, reflecting (i.e., homogeneous Neumann) boundary conditions were imposed.

The geometry shown in Figure 6.3a, with a hemisphere of radius $1\mathrm{m}$, was used. This geometry with a mesh with mesh size $h_s = 0.05\mathrm{m}$ in the hemisphere and $h_p = 0.008\mathrm{m}$ in the pipe was taken to be the base case. Figure 6.3b gives a cross sectional view of the mesh.

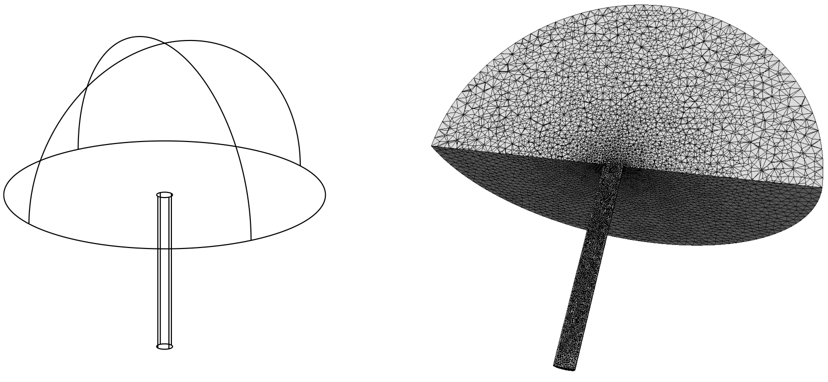

(a) Geometry. **(b)** Cross sectional view of mesh.

Figure 6.3: Geometry and mesh of FEM domain for $r1h_p02$.

The results for this base case were compared to results with meshes on the same geometry, keeping h_s fixed and varying h_p. Further the geometry in Figure 6.4, with hemisphere radius $0.2\mathrm{m}$, was used with $h_p = 0.008\mathrm{m}$ as in the base case, and h_s chosen so that the total number of nodes (and hence the size of the linear system to be solved) would be approximately equal to the base case (60697 nodes for the larger hemisphere and 59101 for the smaller one). We introduce names for the different cases according to Table 6.3.

Table 6.3: Case names for the pipe meshes.

h_p [m]:	0.003	0.004	0.008	0.016
radius $1\mathrm{m}$	$r1h_p3$	$r1h_p4$	$r1h_p8$	$r1h_p16$
radius $0.2\mathrm{m}$			$r02h_p8$	

The simulation was run for frequencies ranging from 76.5Hz to 601Hz (corresponding to wave numbers between 1.4 and 11). In each simulation, i.e., for each frequency, the pipe was driven by point sources of that frequency, outside but near the open end of the pipe. At the resonance fre-

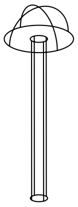

Figure 6.4: Geometry of FEM domain for $r02h_p8$ (see Table 6.3).

quencies, standing waves should then appear in the pipe, and at all other frequencies, the sources should decay rapidly·

Solution visualization Solutions typically look as in Figure 6.5, where a cross sectional view of the imaginary part of the solution for $r1h_p8$ at $f = 580.42$ Hz (near the fourth resonance frequency) is displayed.

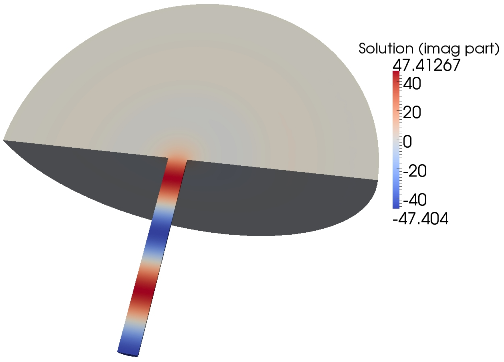

Figure 6.5: Solution (imaginary part) near f_4 for $r1h_p8$.

The solutions along the central axis of the pipe for the first four resonance frequencies are plotted in Figures 6.6-6.9, using the base case mesh $r1h_p8$. The actual length of the pipe is $1\mathrm{m}$, and the effective length L_{eff} is indicated by the solid vertical line. At the chosen frequencies, standing waves appear in the pipe with a node at the open end of the pipe and an anti-node at the closed end.

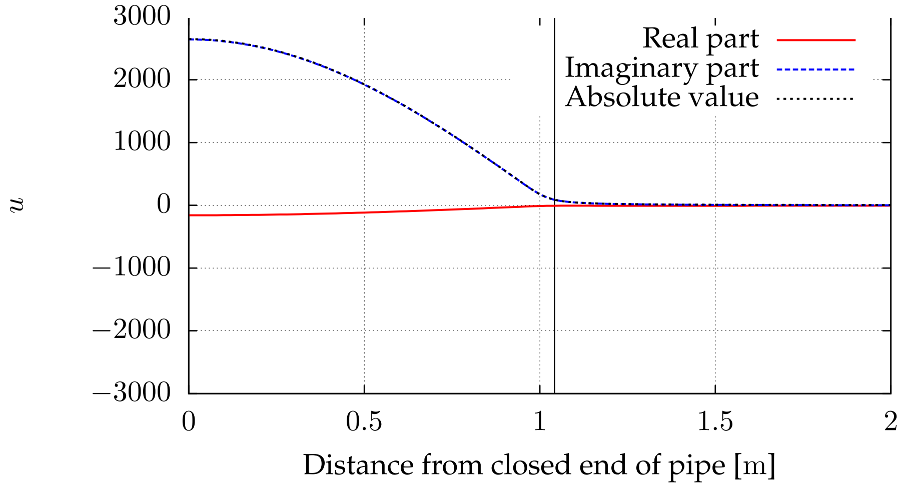

Figure 6.6: Solution along central axis of the pipe at first resonance frequency.

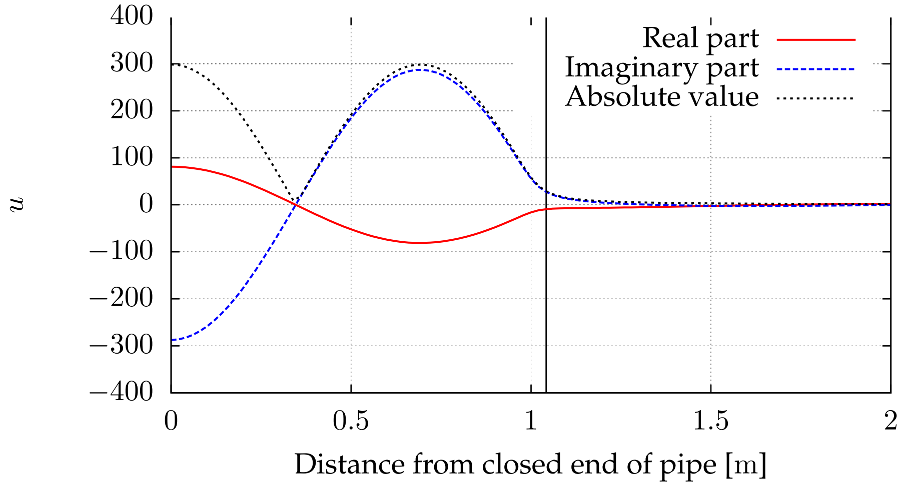

Figure 6.7: Solution along central axis of the pipe at second resonance frequency.

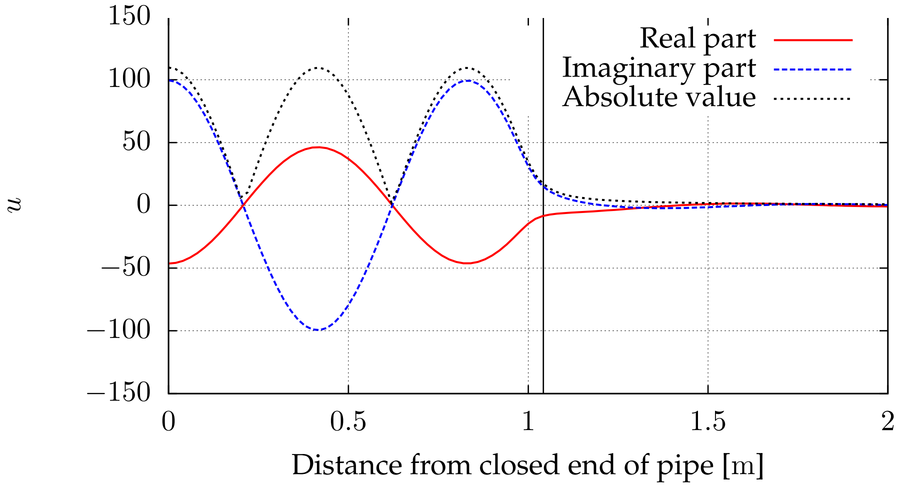

Figure 6.8: Solution along central axis of the pipe at third resonance frequency.

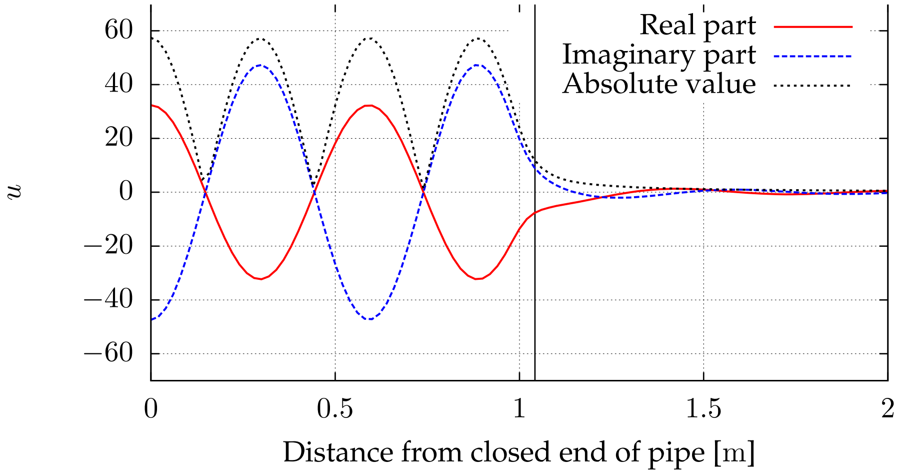

Figure 6.9: Solution along central axis of the pipe at fourth resonance frequency.

Computed resonance frequencies In order to compare the frequencies at which resonance occurs in the simulations to the theoretical values in Table 6.2, the magnitude of the solution was recorded, for each frequency, at the closed end of the pipe, where anti-nodes should appear for standing waves. The results are presented for $r1h_p8$ in Figure 6.10, with solid vertical lines indicating the theoretical resonance frequencies f_1-f_4. We see that the resemblance between theoretical and numerical values is very good.

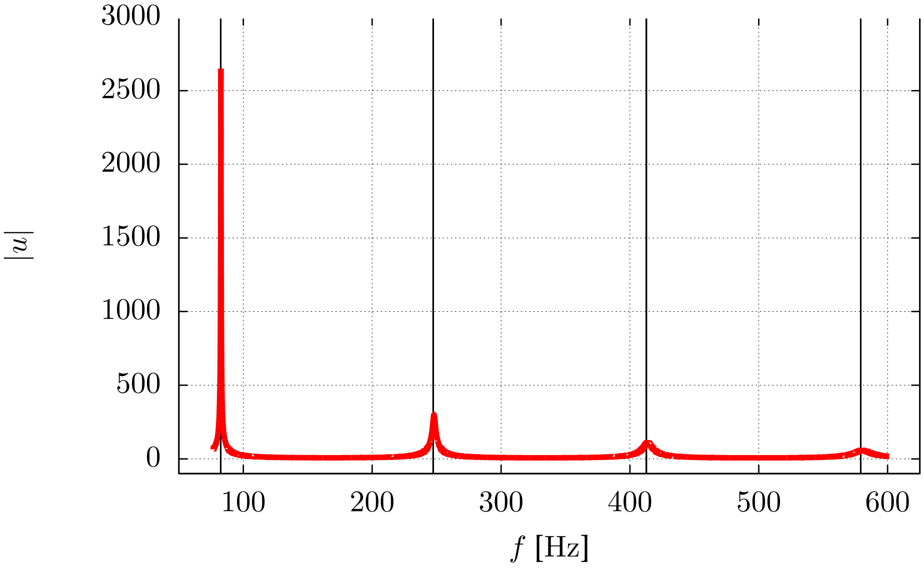

Figure 6.10: Solution (magnitude) for $r1h_p8$ at closed end of pipe, plotted against frequency.

Zooming in around the peaks in Figure 6.10 we can see that the simulations slightly overestimate the resonance frequencies; however, the performance improves when the pipe mesh size h_p is decreased. Results for all five meshes are shown in Figures 6.11 and 6.12 for f_1 and f_2, respectively. We take the numerical approximation of f_m to be the frequency at which the maximal value of the peak nearest f_m is recorded. The numerical approximations of the first four resonance frequencies are listed in Table 6.4

Table 6.4: Numerical approximations of the first four resonance frequencies.

	f_1[Hz]	f_2[Hz]	f_3[Hz]	f_4[Hz]
Theoretical	82.36	247.31	412.82	579.05
$r1h_p16$	82.69	248.68	414.71	581.90
$r1h_p8$	82.58	247.96	413.84	580.42
$r1h_p4$	82.53	247.75	413.46	579.93
$r1h_p3$	82.47	247.69	413.40	579.82
$r02h_p8$	82.42	248.13	414.49	580.75

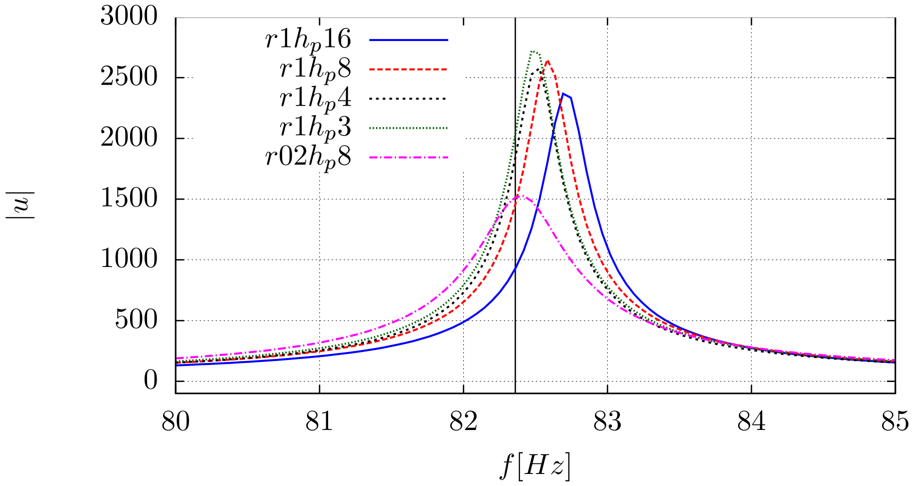

Figure 6.11: Solution (magnitude) at closed end of pipe, near f_1.

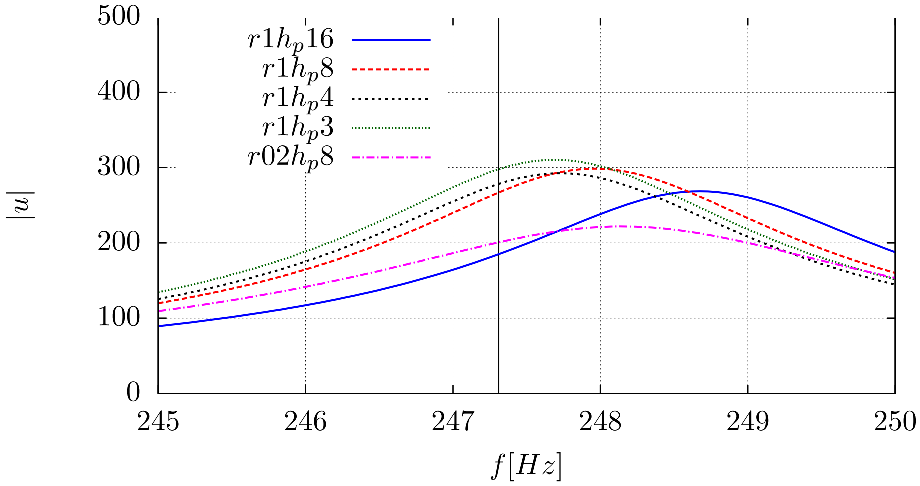

Figure 6.12: Solution (magnitude) at closed end of pipe, near f_2.

Errors in frequency We compute the (absolute) error in frequency by subtracting the theoretical value f_m from the numerical approximation. The errors for the $r1$ cases are plotted against the pipe mesh size in Figure 6.13 and we see a clear convergence with decreasing h_p. On the other hand the error increases with frequency f, which is to be expected, as a finer mesh is needed to resolve waves of higher frequency. Dividing the absolute error by the corresponding resonance frequency f_m we get the relative error, displayed in Figure 6.14 and we see that the error grows roughly linearly with

f. We finally note that with any of the mesh resolutions used, the relative errors are for all four frequencies clearly less than 1%, and with the two finest meshes the errors are even less than 0.2%.

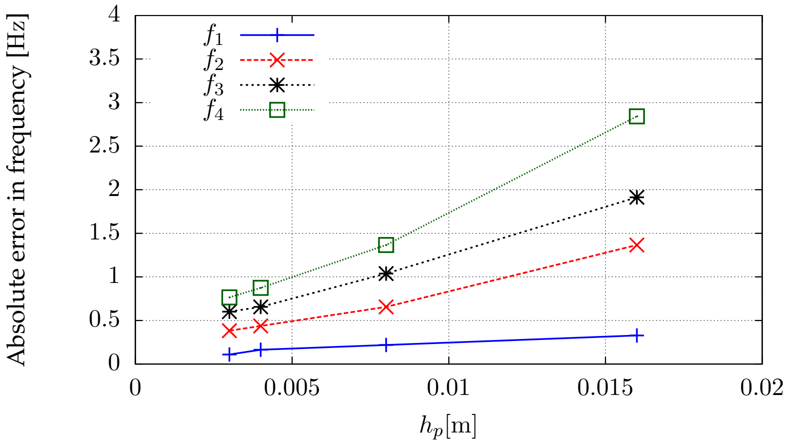

Figure 6.13: Absolute error in frequency for varying mesh sizes in the pipe.

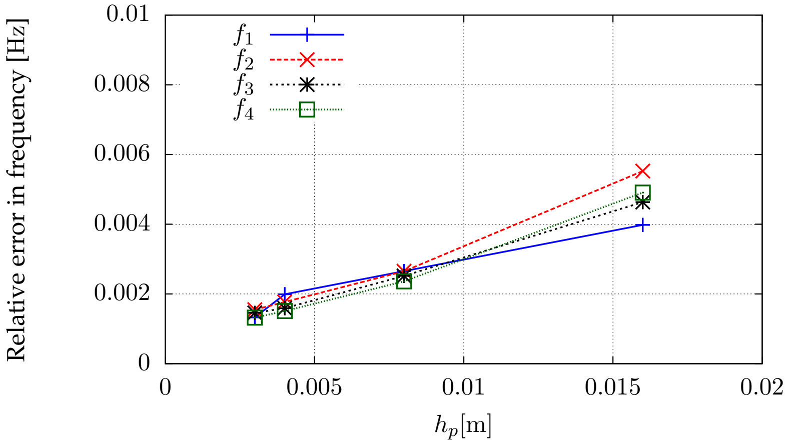

Figure 6.14: Relative error in frequency for varying mesh sizes in the pipe.

The results do not seem to be very sensitive to the choice of cut-off radius, at which finite elements are coupled to infinite elements, as long as the total number of degrees of freedom is kept roughly constant. The error in frequency for $r02h_p8$ is very small at f_1, as can be seen in Table 6.4. However, at f_2-f_4 the error in frequency for $r02h_p8$ stays between the errors for $r1h_p8$ and $r1h_p16$.

All of the above tests were performed using infinite element radial basis functions of order 1. Preliminary tests performed indicate no improvement using higher radial orders.

6.3 Tones from Flow Past a Deep Cavity

So far, the test cases have been treating the Helmholtz equation (6). We now come to a case in which sound sources are computed from the solution of the Navier-Stokes equations, i.e., we consider the reduced form of Lighthill's analogy (7). The geometry is fixed, so we need only consider *volumetric* source terms (i.e., the volume integral in (13)).

The test case exhibits some similarities with the pipe case; again we consider resonance at certain frequencies, however in this case the pipe is replaced by a deep cavity with a rectangular cross section. Shear flow over the cavity results in flow oscillations which in turn give rise to sound waves. A detailed investigation of such a simulation has been made in [5], where simulation results are compared to experimental results from [41] (see also [42]).

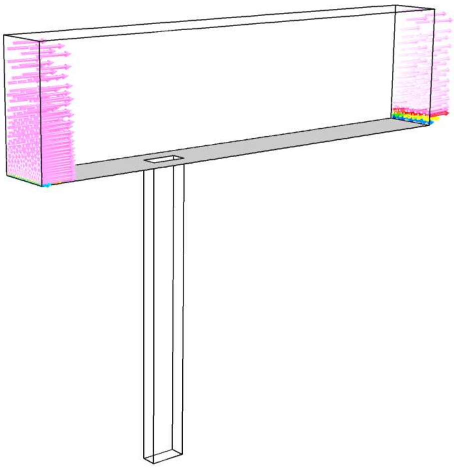

Figure 6.15: Geometry of the CFD domain. Inlet velocity $18.3\mathrm{m/s}$.

CFD simulation The geometry for the CFD simulation is shown in Figure 6.15, with arrows indicating the flow direction. The cavity has the same dimensions as in [5], i.e., width $L_\mathrm{w} = 0.0254\mathrm{m}$, streamwise length $L_\mathrm{s} = 0.058\mathrm{m}$ and depth $L_\mathrm{d} = 0.4826\mathrm{m}$. An isentropic form of the pseudo-compressible Navier-Stokes equations was solved using the AcuSolve™ [1] CFD software with DES[3]. The velocity was set to $18.3\mathrm{m/s}$ at the inlet, no-slip conditions (i.e., $\boldsymbol{v} = 0$) were imposed on all sides of the cavity and on the "floor" (gray in Figure 6.15), and slip-conditions (i.e., $\boldsymbol{v} \cdot \boldsymbol{n} = 0$) were imposed on the side and top walls. At the outlet the pressure was set to zero, under the simplifying assumption of no gravity.

---

[3] Detached eddy simulation; RANS (Reynolds-averaged Navier-Stokes) equations near boundaries and LES (large eddy simulation) away from boundary layers.

The CFD computation was run with four CPU cores on a coarse mesh ($4.3 \cdot 10^6$ tetrahedra, $7.7 \cdot 10^5$ nodes) with a time step $\Delta t = 10^{-4}$s. Once a pseudo-steady flow condition was reached, the simulation was run - and results recorded - for 4096 time steps, i.e., the total recorded simulation time was $T = 0.4096$s, which corresponds to a step size of $\Delta f = 1/T \approx 2.44$Hz in the frequency domain.

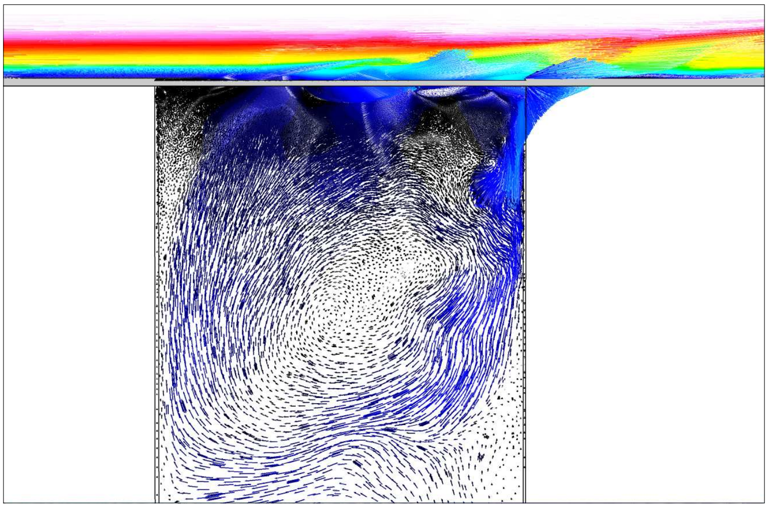

Figure 6.16: Velocity at cross section parallel to flow direction. Colored with velocity magnitude: black: 0m/s, white: ≥ 18m/s.

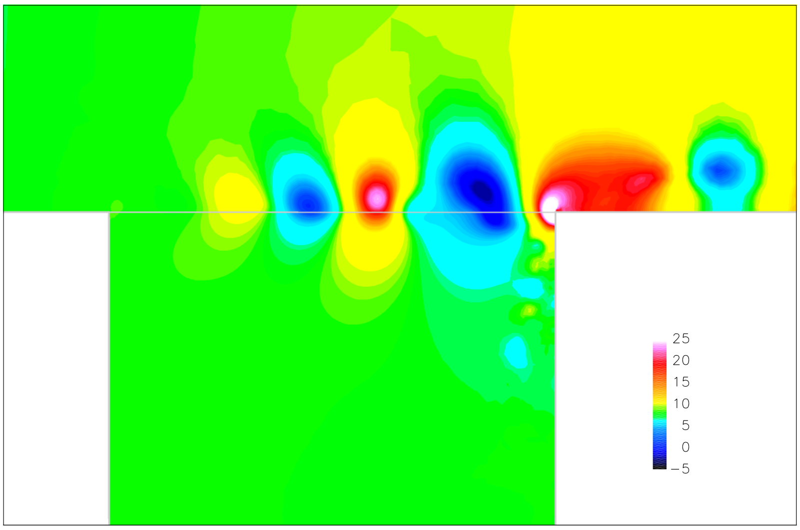

Figure 6.17: Pressure fluctuations [Pa] around $p_0 = 101325$Pa. Displayed at cross section parallel to flow direction.

Snapshots of the pseudo-steady flow are displayed in Figures 6.16–6.19 at cross sections near the opening of the cavity. Figures 6.16 and 6.17 show the velocity and pressure fields, respectively, at a cross section parallel to the flow direction. In Figures 6.18 and 6.19, the velocity field and magnitude are displayed at a cross section normal to the flow direction.

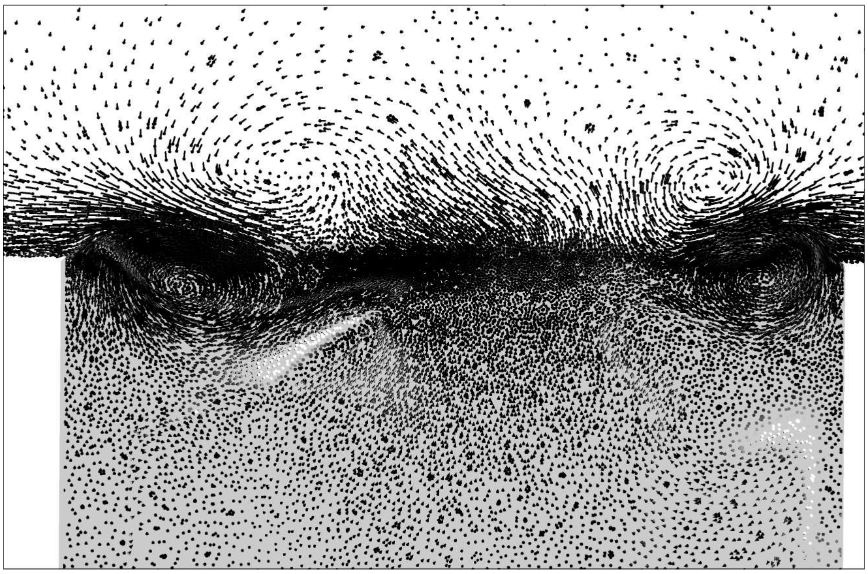

Figure 6.18: Velocity at cross section normal to flow direction.

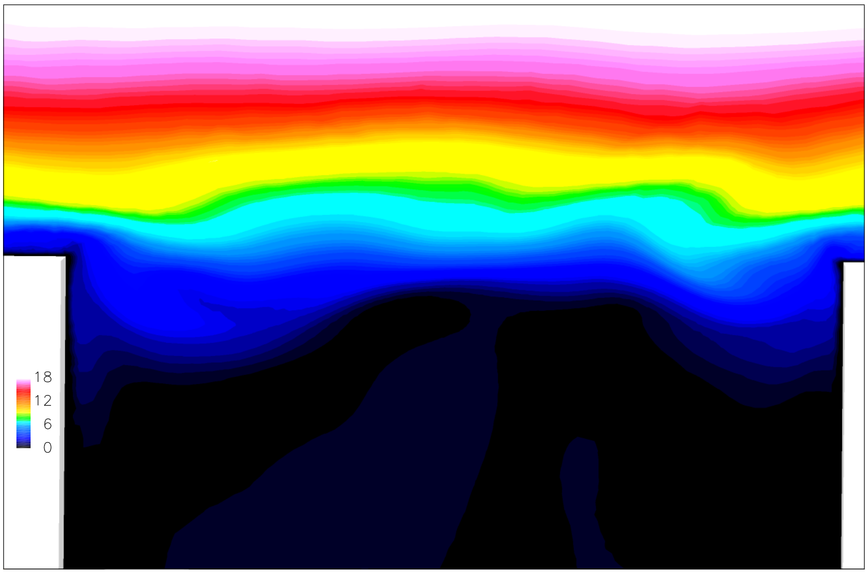

Figure 6.19: Velocity magnitude [m/s] at cross section normal to flow direction.

Acoustic sources The source terms for the acoustic solver take the form

$$L_{\mathrm{L}}(\varphi_k) = -\frac{1}{a_0^2} \sum_{i=1}^{d} \sum_{j=1}^{d} \int_{\Omega} \frac{\partial T_{ij}}{\partial x_j} \frac{\partial \bar{\varphi}_k}{\partial x_i} \, \mathrm{d}\Omega,$$

where φ_k are nodal basis functions corresponding to the acoustic mesh. The simplified form (4) of Lighthill's tensor was used, and the source terms were computed in AcuSolve™. Figure 6.20 shows the source strength in terms of $|\nabla \cdot \boldsymbol{T}|$ at a cross section parallel to the flow direction, near the cavity opening. Isosurfaces for $|\nabla \cdot \boldsymbol{T}| = 6000\mathrm{Pa/m}$ are shown in Figure 6.21, viewing the cavity opening from above with flow direction from left to right.

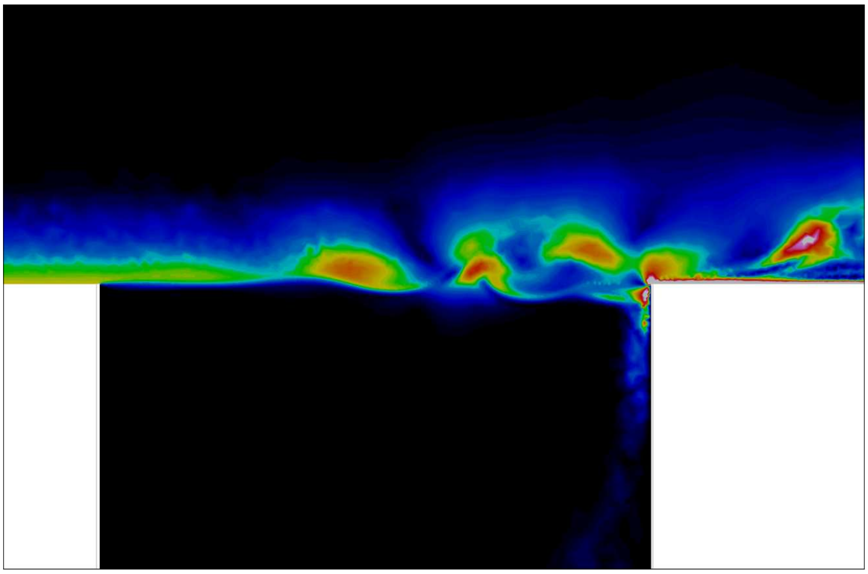

Figure 6.20: Source strength in terms of $|\nabla \cdot \boldsymbol{T}|$ at a cross section parallel to the flow direction, near the cavity opening. Coloring: black: $0\mathrm{Pa/m}$, white: $10\,000\mathrm{Pa/m}$.

Sources were expected to appear near the cavity opening but to be of negligible size a distance away from there. Hence, in order to reduce the amount of stored data, source terms were computed only for nodal basis functions having support within a given domain near the opening, see Figure 6.22. Figures 6.20 and 6.21 confirm the assumption that sources are strongest near the cavity opening, particularly at its rear side. Inspecting a larger cross section, it was noticed that beyond the rear end of the opening, the sources were stronger than expected, so that they should have been recorded in a larger region. This may lead to a source of error in the results presented here.

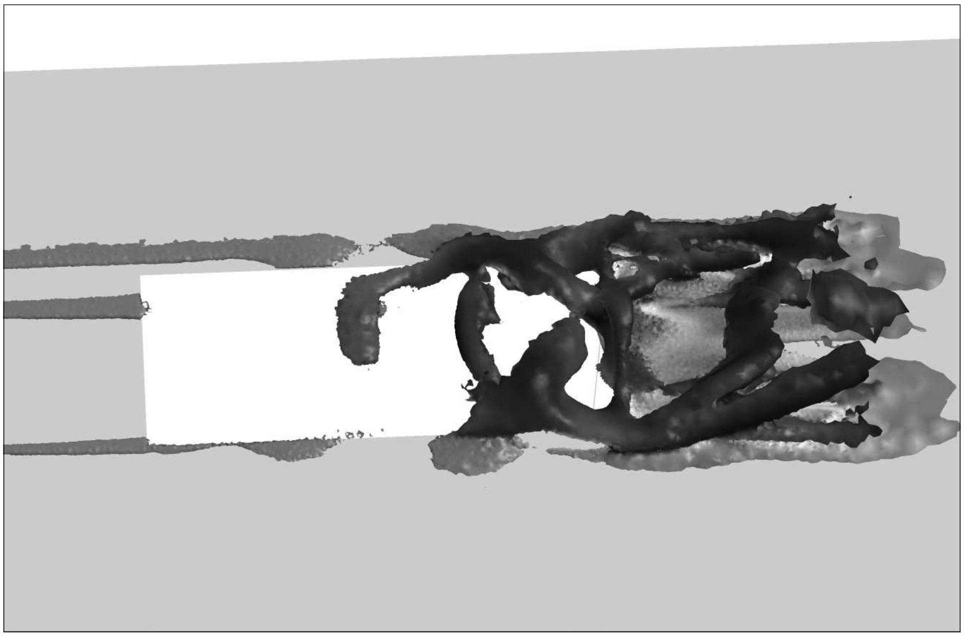

Figure 6.21: Isosurface for $|\nabla \cdot \boldsymbol{T}| = 6000\mathrm{Pa/m}$ near the cavity opening. Colored by vorticity (absolute value).

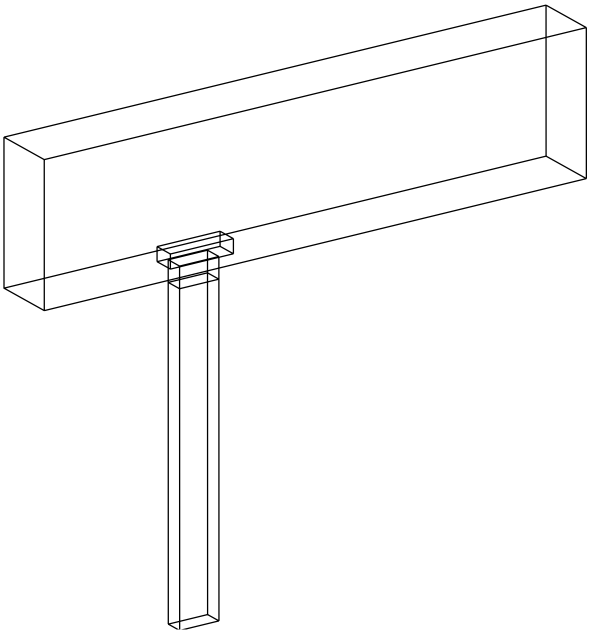

Figure 6.22: Geometry of the CFD domain. The region in which acoustic sources were recorded is indicated by the "boxes" near the cavity opening.

Acoustic simulation In Figure 6.23, the domain of the CFD computation (cf. Figures 6.15 and 6.22) is shown together with the acoustic domain. The latter consists of the cavity and the hemisphere of radius 1.5m, beyond which infinite elements were used.

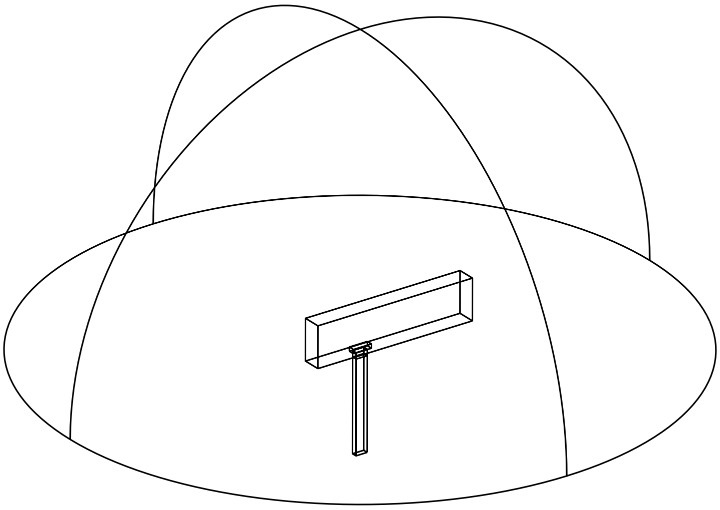

Figure 6.23: Geometry of the CFD and acoustic domains.

Acoustic resonance is expected (as in the pipe case) to occur in the cavity for certain acoustic mode frequencies, approximately computed as

$$f_m = \frac{2m-1}{4}\frac{a_0}{L_\mathrm{d}+\Delta}, \qquad m = 1, 2, \ldots, \tag{47}$$

(cf. (46)), where $L_\mathrm{d} = 0.4826\mathrm{m}$ is the cavity depth and the correction Δ was determined in [5] to be approximately one inch, i.e. $0.0254\mathrm{m}$, based on experimental values for a cavity with the same dimensions as the one used here. Inserting these values into (47), we expect the first three acoustic modes to appear approximately at frequencies

$$\begin{aligned} f_{a1} &\approx 169\,\mathrm{Hz}, \\ f_{a2} &\approx 507\,\mathrm{Hz}, \\ f_{a3} &\approx 845\,\mathrm{Hz}. \end{aligned}$$

In [5], results from physical experiments are presented, in which the pressure was measured at the bottom of the cavity. The results from the acoustic simulation using caaHelmholtz were recorded at two nodes on the cavity bottom as well as at six nodes on the hemisphere, i.e., 1.5m from the cavity opening. As no significant differences appeared between the two nodes at the cavity bottom, nor between the six nodes at the hemisphere, results are presented only for one cavity bottom node and one hemisphere node. These simulation results are presented in Figure 6.24 together with experimental data recovered from [5]. The first three acoustic modes are indicated by solid vertical lines.

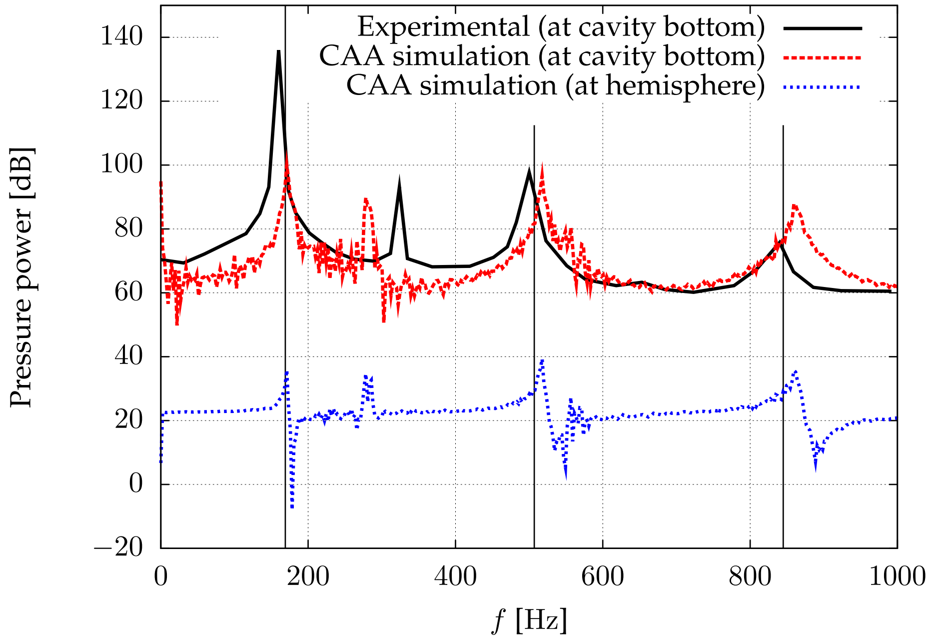

Figure 6.24: Acoustic pressure power spectrum. Experimental data recovered from [5] (Figure 6a).

The overall features of the experimental data are well resembled by the simulation. The magnitude is underestimated by the simulation at the first acoustic mode and somewhat overestimated at the third one, but is fairly correct elsewhere. As expected, a much smaller magnitude is recorded at the hemisphere, $1.5\mathrm{m}$ from the cavity than at the cavity bottom. It should be noted that the mesh used for the CFD computation was much coarser than meshes normally used for CAA simulations, and that the time window was short, about $0.4\mathrm{s}$. Hence, errors are expected, but in relation to the low computational cost, the accuracy of the simulation is very good. With a finer CFD mesh it is likely that the magnitude would be more accurately captured also at the first and third acoustic mode. No GLS stabilization was used in the acoustic computation, so dispersion errors are expected. As was previously mentioned, the region in which acoustic sources were recorded might have been too narrow, so that relevant sources outside that region were neglected. Recording sources in a larger region, especially downstream the cavity opening, might further improve the simulation results.

As in the pipe case, the frequencies of acoustic modes are well predicted by the simulation. As expected, the best accuracy is achieved at the first mode; a finer mesh would be needed to reach the same accuracy at higher frequencies.

The magnitude of the solution, i.e., of $\tilde{\varrho}_a$, at the third acoustic mode is shown in Figure 6.25 at a cross section of the FEM domain. The cross section is parallel to the flow direction, with flow from left to right. There is a standing wave in the cavity with an anti-node at the cavity bottom. Outside the cavity the magnitude decays rapidly (note that a logarithmic scale is used). Zooming in at the cavity opening, see Figure 6.26, we note that there are fluctuations at the rear end of the opening, corresponding to the region where sources are strongest, cf. Figure 6.20.

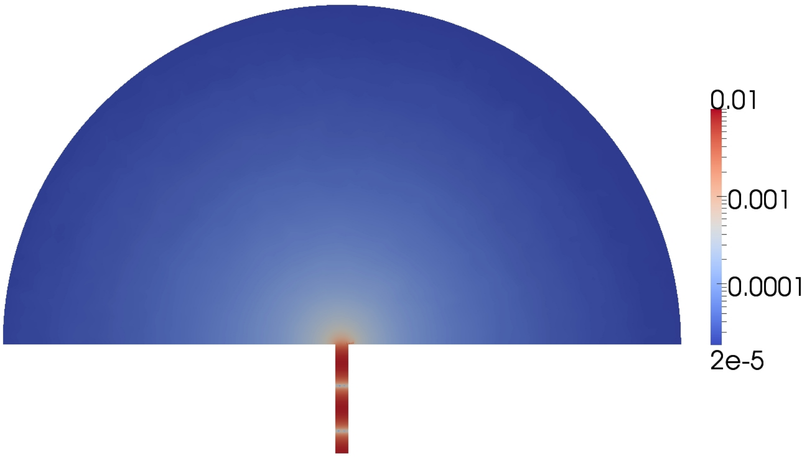

Figure 6.25: Magnitude of reduced acoustic density ($|\tilde{\varrho}_a|$) at third acoustic mode. Displayed at a cross section (of the acoustic FEM domain) parallel to the flow direction, with flow from left to right. Note that a logarithmic scale is used.

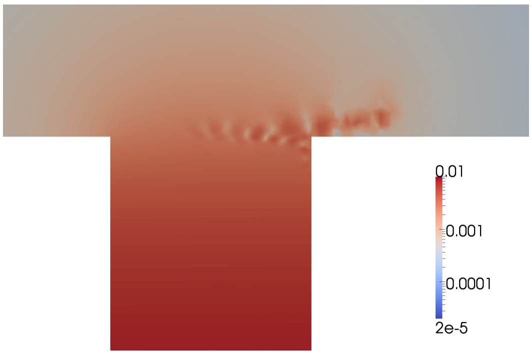

Figure 6.26: Magnitude of reduced acoustic density ($|\tilde{\varrho}_a|$) at third acoustic mode. Displayed at a cross section parallel to the flow direction, near the cavity opening, with flow from left to right. Note that a logarithmic scale is used.

7 Summary and Future Work

To solve the compressible Navier-Stokes equations would be an accurate, but in a real situation too computationally expensive method to predict sound pressure levels caused by transient fluid flows. A less costly alternative, a hybrid computational aero-acoustics (CAA) methodology, has been suggested in the literature, where the incompressible or compressible Navier-Stokes equations are solved on a much coarser mesh than would be needed for capturing acoustic fluctuations. The velocity and pressure fields are then used to compute acoustic sources in divergence form. In a second step of the hybrid methodology, the sources are propagated in space by a special form of the Helmholtz equation, namely the reduced form of Lighthill's analogy.

The solver caaHelmholtz, that was developed in this work, solves the Helmholtz equation, optionally with the right hand side from Lighthill's analogy. The acoustic solver is coupled with a CFD solver to perform three-dimensional CAA computations using the described hybrid methodology.

For the test cases presented in Section 6 the solver performed well. In particular, the frequencies at which standing waves appear in a pipe or deep cavity were predicted with good accuracy by the simulations. In the cavity case, caaHelmholtz was used with sources from a CFD simulation, showing the feasibility of the hybrid CAA methodology.

Some work remains to validate the accuracy of the implementation, including its ability to correctly predict not only resonance frequencies, but also the actual sound pressure levels. Once the implementation has been properly validated, the following improvement suggestions may be considered:

(i) The program can be improved by a better treatment of complex linear systems. In the current implementation, a linear system of twice the number of degrees of freedom is solved for complex valued matrices. Using a solver that handles complex numbers would reduce the required storage and possibly the computational time.

(ii) With the Galerkin/least-squares (GLS) method, good stabilization is achieved only if the characterizing parameter τ is well chosen, with respect to the used mesh. The formula to compute τ used in the current implementation, was originally developed for the 2D Helmholtz equation, rather than the 3D case. The sensitivity of the choice of τ has not been evaluated, and fine-tuning this parameter might improve the GLS stabilization.

(iii) Developing a framework for a more automated pre- and post-processing of data would simplify the use of the program.

8 Division of Work

The program caaHelmholtz has been developed by the author, using a basic framework for containers and data structures developed at and provided by FCC. The program is based on a finite element method for interior problems, i.e., problems on a bounded domain, and in the current implementation piecewise linear basis functions are used. The standard Galerkin method as well as the stabilized Galerkin/least-squares (GLS) method are implemented. To handle exterior problems, i.e., problems on an unbounded domain, a coupled finite-infinite element method is implemented, using trial and test spaces of conjugated Astley-Leis type for the infinite elements.

Several simulations using caaHelmholtz have been run by the author. Results are presented in Section 6 for three cases: (i) Plane wave in box, (ii) Resonance in pipe and (iii) Tones from flow past a cavity.

Dr. Robert Sandboge has contributed to the work by setting up all 3D geometries, writing pre-processors to produce input data to caaHelmholtz, including transformation by the FFT of data from CFD computations, and helping the author in running CFD computations for the cavity case. These contributions are gratefully acknowledged.

A Running caaHelmholtz: Input and Output

The program caaHelmholtz is run with one input argument and optional flags:

```
caaHelmholtz [options] filename.inp
```

where `filename.inp` is the name of a file containing parameter values specifying the problem and the numerical methods to be used. Available options are described in Section A.1 and the contents of the input file in Section A.2

A.1 Options

The following options may be used with caaHelmholtz:

```
-d d_value
-i "keyword file_name"
-k k_value
-n n_value
-R
-w
```

-d, -k and -n Options `-d`, `-k` and `-n` are used to loop over a set of wave numbers k. The program is run for `n_value` different values of k, starting with k = `k_value` and in each iteration adding `d_value` to k. Default values are

```
k_value = 0
n_value = 1
d_value = 1
```

The default value for `k_value` is used only if the `-k` option is not used and no value for k has been specified in the input file (`filename.inp`, see Table A.1). If a value for k is specified in the input file *and* by the `-k` option, the `-k` option value is used.

-i Use option `-i` to override a line in the input file `filename.inp`. The `keyword` may be one of the following:

```
source_volume_helmholtz_file
source_volume_lighthill_file
source_surface_quad_rule_file
source_surface_values_file
source_surface_elements_file
```

and should be followed by the name of the corresponding data file.

-R Use option `-R` (right hand side) to output the right hand side vector without solving the linear system. **Note:** The `-R` option overrides any solution output options; the solution is not computed and hence cannot be output.

-w Use option `-w` (write) to output the solution (at all nodes) in `vtk` file format.

A.2 Input Files

The input file `filename.inp` should have the format shown in Table A.1.

Table A.1: Format of the input file `filename.inp`.

```
k                                     val_k
a0                                    val_a0
stabilization                         val_stab
IE_center                             x0 y0 z0
IE_radial_order                       val_ie_ord
output_node                           n1
output_node                           n2
⋮                                     ⋮
linear_solver_method                  ls_method
linear_solver_preconditioner          ls_pc
linear_solver_tolerance               ls_tol
linear_solver_max_iterations          ls_max_iter
linear_solver_matrix_block_structure  ls_mbstruct

size_data_file                        sizes.dat
coordinate_file                       file.crd
volume_element_file                   tet.cnn
boundary_element_file                 tri.srf
source_volume_helmholtz_file          vol_helm.dat
source_volume_lighthill_file          vol_light.dat
source_surface_quad_rule_file         surf_quad.dat
source_surface_values_file            surf_val.dat
source_surface_elements_file          surf_elem.dat
infinite_element_file                 ie.ies
BC_dirichlet_strong_file              dir_strong.nbc
BC_neumann_file                       neumann.ebc
BC_robin_file                         robin.ebc
```

The meaning of the parameters in the first ten lines are specified in Table A.2, along with listings of values they can take on. The contents of the data files specified in the input file (see Table A.1) are described in Table A.3 and the formats of the individual files are shown in Tables A.7a-A.13. In general, `e` refers to a volume element (tetrahedron), `s` refers to a surface element (triangle) and `n` refers to a node.

Table A.2: Parameters to be specified in the input file.

Parameter	Explanation	Accepted values (default shown in bold type)
`val_k`	Wave number for which to solve Helmholtz equation	Any non-negative real number (**0**)
`val_a0`	Speed of sound (in m/s) in the fluid at rest. Must be specified (only) if surface or volume sources of Lighthill type are given	Any non-negative real number (**343.4**, corresponding to air at 20°C)
`val_stab`	Stabilization method	′**none**′ or ′gls′ (Galerkin/Least-Squares)
`x0 y0 z0`	Coordinates of the center of the set of infinite elements	Real valued coordinates specifying a point with approximately the same distance to any surface element in the corresponding `ie.ies` file
`val_ie_ord`	Maximal order of the radial basis functions on infinite elements	Any positive integer (**1**)
`n1,n2,...`	Nodes at which the solution is output to file (one file per node)	Any integer between 1 and the number of mesh nodes (by default no output)
`ls_method`	Method to be used when solving the linear system	′**direct**′ or ′gmres′
`ls_pc`	Preconditioner to be used when solving the linear system	′**MKL_PC_NONE**′ or ′MKL_PC_ILU0′
`ls_tol`	Tolerance to be used when solving the linear system	Any positive real number (**1.e-12**)
`ls_max_iter`	Maximum number of iterations to be performed when solving the linear system	Any positive integer (**1000**)
`ls_mbstruct`	Matrix block structure to be used when solving the linear system (only in case of complex matrix)	′**full**′ or ′schur′

Table A.3: Description of data files specified in the input file.

File name	Description
`sizes.dat`	Specification of number of dimensions, nodes, volume elements, boundary elements and infinite element boundary elements.
`file.crd`	Mesh node coordinates
`tet.cnn`	Mesh tetrahedra specified by corner node indices
`tri.srf`	Boundary elements (triangles) specified by parent element (tetrahedron) and corner nodes
`vol_helm.dat`	Volumetric sources of type f in (6) specified by node
`vol_light.dat`	Volumetric sources of the type in (7), given as $(\sum\sum\int_\Omega \frac{\partial \tilde{T}_{ij}}{\partial x_j}\frac{\partial \bar{v}}{\partial x_i}\,\mathrm{d}\Omega)$ specified by nodal test function
`surf_quad.dat`	Quadrature rule used for surface sources
`surf_val.dat`	Surface source values (i.e., $\sum\sum \frac{\partial \tilde{\Sigma}_{ij}}{\partial x_j} n_i$) specified at quadrature points
`surf_elem.dat`	Elements at which surface sources are specified
`ie.ies`	Surface elements to which infinite elements should be coupled
`dir_strong.nbc`	Dirichlet boundary conditions to be imposed strongly, specified by node
`neumann.ebc`	Neumann boundary conditions specified by element
`robin.ebc`	Robin boundary conditions specified by element

Table A.4: Format of `sizes.dat`. See Table A.5 for explanations to the parameters.

`dimension`	`d`
`nMeshNodes`	`nMN`
`nMeshTets`	`nMTe`
`nMeshTris`	`nMTR`
`nIENodes`	`nIEN`

Table A.5: Parameters to be specified in `sizes.dat`.

Parameter	Explanation	Accepted values
`d`	Number of spatial dimensions	Non-negative integer
`nMN`	Number of mesh nodes	Non-negative integer, must match the number of lines in file `file.crd`
`nMTe`	Number of volume elements	Non-negative integer, must match the number of lines in file `tet.cnn`
`nMTr`	Number of boundary elements	Non-negative integer, must match the number of lines in file `tri.srf`
`nIEN`	Number of boundary nodes coupled to infinite elements	Non-negative integer, must match the number of nodes belonging to surface elements specified in file `ie.ies`

Table A.6: Mesh file formats.

n1	x1	y1	z1
n2	x2	y2	z2
⋮	⋮	⋮	⋮

(a) Format of `file.crd`.

e1	$\mathtt{n}_{j1}$	$\mathtt{n}_{j2}$	$\mathtt{n}_{j3}$	$\mathtt{n}_{j4}$
e2	$\mathtt{n}_{j5}$	$\mathtt{n}_{j6}$	$\mathtt{n}_{j7}$	$\mathtt{n}_{j8}$
⋮	⋮	⋮	⋮	⋮

(b) Format of `tet.cnn`.

s1	$\mathtt{e}_{j1}$	$\mathtt{n}_{k1}$	$\mathtt{n}_{k2}$	$\mathtt{n}_{k3}$
s2	$\mathtt{e}_{j2}$	$\mathtt{n}_{k4}$	$\mathtt{n}_{k5}$	$\mathtt{n}_{k6}$
⋮	⋮	⋮	⋮	⋮

(c) Format of `tri.srf`.

Table A.7: Format of `vol_helm.dat`. The lines should correspond to the lines in `file.crd` (in the same order). The third column is optional.

$\mathtt{n}_1$	$\mathtt{real\_f}_1$	$\mathtt{imag\_f}_1$
$\mathtt{n}_2$	$\mathtt{real\_f}_2$	$\mathtt{imag\_f}_2$
⋮	⋮	⋮

Table A.8: Format of `vol_light.dat`.

$\mathtt{n}_{j1}$	$\mathtt{real\_val}_{j1}$	$\mathtt{imag\_val}_{j1}$
$\mathtt{n}_{j2}$	$\mathtt{real\_val}_{j2}$	$\mathtt{imag\_val}_{j2}$
⋮	⋮	⋮

Table A.9: Format of `surf_quad.dat`. The first column specifies weights and the last three define coordinates of the corresponding quadrature points on the master triangle. The weights must sum to 1.

$\mathtt{w}^{(1)}$	$\xi_1^{(1)}$	$\xi_2^{(1)}$	$\xi_3^{(1)}$
$\mathtt{w}^{(2)}$	$\xi_1^{(2)}$	$\xi_2^{(2)}$	$\xi_3^{(2)}$
$\vdots$	$\vdots$	$\vdots$	$\vdots$

Table A.10: Format of `surf_val.dat`. $\mathtt{val}_{k,l}$ specifies the value of $\sum\sum \frac{\partial\tilde{\Sigma}_{ij}}{\partial x_j} n_i$ at quadrature point l (as specified in `surf_quad.dat`) of surface source element k (as specified in `surf_elem.dat`).

$\mathtt{real\_val}_{1,1}$	$\mathtt{imag\_val}_{1,1}$
$\mathtt{real\_val}_{1,2}$	$\mathtt{imag\_val}_{1,2}$
$\vdots$	$\vdots$
$\mathtt{real\_val}_{1,n_{int}}$	$\mathtt{imag\_val}_{1,n_{int}}$
$\mathtt{real\_val}_{2,1}$	$\mathtt{imag\_val}_{2,1}$
$\vdots$	$\vdots$

Table A.11: Format of `surf_elem.dat` and `ie.ies`. In `surf_elem.dat`, $\mathtt{s}_{ji}$ specifies surface elements at which surface sources are specified in `surf_val.dat`. In `ie.ies`, they specify surface elements at which infinite elements should be used.

$\mathtt{s}_{j1}$
$\mathtt{s}_{j2}$
$\vdots$

Table A.12: Format of `dirichlet_strong.nbc`. The third column is optional.

$\mathtt{n}_{j1}$	$\mathtt{real\_val}_{j1}$	$\mathtt{imag\_val}_{j1}$
$\mathtt{n}_{j2}$	$\mathtt{real\_val}_{j2}$	$\mathtt{imag\_val}_{j2}$
$\vdots$	$\vdots$	$\vdots$

Table A.13: Format of `neumann.ebc` and `robin.ebc`. The values $\mathtt{real\_val}_{j1}$ and $\mathtt{imag\_val}_{j1}$ specify real and imaginary part of Neumann ($\frac{\partial u}{\partial n} = \mathtt{val}$) and homogeneous Robin ($\mathtt{val}u + \frac{\partial u}{\partial n} = 0$) boundary condition values at boundary element $\mathtt{s}_{ji}$, respectively. The third column is optional.

$\mathtt{s}_{j1}$	$\mathtt{real\_val}_{j1}$	$\mathtt{imag\_val}_{j1}$
$\mathtt{s}_{j2}$	$\mathtt{real\_val}_{j2}$	$\mathtt{imag\_val}_{j2}$
$\vdots$	$\vdots$	$\vdots$

References

[1] AcuSolve™, *CFD software*, Altair Engineering, Inc., 1820 Big Beaver Rd, Troy, MI 48083, USA. (Previously owned by ACUSIM Software.)

[2] Astley R.J and Coyette J.-P., *Conditioning of infinite element schemes for wave problems*, Commun. Numer. Mech. Engng., Vol. 17, pp. 31-41 (2001).

[3] Astley R.J., Macaulay G.J., Coyette J.-P. and Cremers L., *Three-dimensional wave-envelope elements of variable order for acoustic radiation and scattering. I. Formulation in the frequency domain*, J. Acoust. Soc. Am., Vol. 103, pp. 49-63 (1998).

[4] Atkinson F.V., *On Sommerfeld's radiation condition*, Philos. Mag., Vol. 40, pp. 645-51 (1949).

[5] Bagwell T.G., *CFD simulation of flow tones from grazing flow past a deep cavity*, Proceedings of IMECE06, 2006 ASME International Mechanical Engineering Congress and Exposition, 5-10 November 2006, Chicago, Illinois, USA (2006).

[6] Bayliss A. and Turkel E., *Radiation boundary conditions for wave-like equations*, Commun. Pure Appl. Math., Vol. 33, pp. 707-725 (1980).

[7] Bettess P., *Infinite elements*, Int. J. Numer. Methods Eng., Vol. 11, pp. 53-64 (1977).

[8] Bettess P., *Infinite Elements*, Sunderland: Penshaw Press (1992).

[9] Burnett D.S., *A 3-D acoustic infinite element based on a generalized multipole expansion*, J. Acoust. Soc. Am., Vol. 96, pp. 2798-2816 (1994).

[10] Burnett D.S. and Holford R.L., *Prolate and oblate spheroidal acoustic infinite elements*, Comput. Methods Appl. Mech. Eng., Vol. 158, pp. 117-142 (1998).

[11] Burnett D.S. and Holford R.L., *An ellipsoidal acoustic infinite element*, Comput. Methods Appl. Mech. Eng., Vol. 164, pp. 49-76 (1998).

[12] Caro S., Ploumhans P., Gallez X., Sandboge R., Shakib F. and Matthes M., *A new CAA formulation based on Lighthill's analogy applied to an idealized automotive HVAC blower using AcuSolve and Actran/LA*, AIAA/CEAS 11th Aeroacoustic Conference, 23-25 May 2005, Montery, California, USA, AIAA Paper 2005-3015 (2005).

[13] Caro S., Sandboge R., Iyer J. and Nishio Y., *Presentation of a CAA formulation based on Lighthill's analogy for fan noise*, Fan Noise 2007 Conference, 17-19 September 2007, Lyon, France.

[14] Engquist B. and Majda A., *Absorbing boundary conditions for the numerical simulation of waves*, Math. Comput., Vol. 31, pp. 629-651 (1977).

[15] Engquist B. and Majda A., *Radiation boundary conditions for acoustic and elastic wave calculations*, Commun. Pure Appl. Math., Vol. 32, pp. 313-357 (1979).

[16] Feng Kang, *Finite element method and natural boundary reduction*, Proceedings of the International Congress of Mathematicians, Warsaw, pp. 1439-1453 (1983).

[17] Gmsh©, *Mesh generation software*, http://geuz.org/gmsh/.

[18] Gnuplot©, *Visualization software*, http://www.gnuplot.info/.

[19] Harari I. and Hughes T.J.R., *Finite element methods for the Helmholtz equation in an exterior domain: Model problems*, Comput. Methods Appl. Mech. Engrg., Vol. 87, pp. 59-96 (1991).

[20] Harari I. and Hughes T.J.R., *Galerkin/least-squares finite element methods for the reduced wave equation with non-reflecting boundary conditions in unbounded domains*, Comput. Methods Appl. Mech. Engrg., Vol. 98, pp. 411-454 (1992).

[21] Harari I. and Nogueira C.L., *Reducing dispersion of linear triangular elements for the Helmholtz equation*, J. Engrg. Mech., Vol. 128, pp. 351-358 (2002).

[22] Hughes T.J.R., *The Finite Element Method: Linear Static and Dynamic Finite Element Analysis*, N.Y.: Dover (2000).

[23] Hughes T.J.R., Reali A. and Sangalli G., *Duality and unified analysis of discrete approximations in structural dynamics and wave propagation: Comparison of p-method finite elements with k-method NURBS*, Comput. Methods Appl. Mech. Engrg., Vol. 197, pp. 4104-4124 (2008).

[24] Ihlenburg F., *Finite Element Analysis of Acoustic Scattering*, New York: Springer (1998).

[25] Intel® Math Kernel Library, *Computing math library*, Intel Corporation, 2200 Mission College Blvd., Santa Clara, CA 95052-8119, USA.

[26] Kinsler L.E., Frey A.R., Coppens A.B. and Sanders J.V., *Fundamentals of Acoustics*, 4th ed., John Wiley & Sons (2000).

[27] Leis R., *Initial Boundary Value Problems in Mathematical Physics*, Stuttgart: Teubner (1986).

[28] Lighthill M.J., *On sound generated aerodynamically*, Proc. Roy. Soc. Lond. A, Vol. 211, pp. 564-587 (1952).

[29] MATLAB®, *High-level programming language*, MathWorks®, 3 Apple Hill Drive, Natick, MA 01760-2098, USA.

[30] Oberai A. and Pinsky, P.M., *A multiscale finite element method for the Helmholtz equation*, Comput. Methods Appl. Mech. Engrg., Vol. 154, pp. 281-297 (1998).

[31] Oberai A., Roknaldin F. and Hughes T., *Computational procedures for determining structural-acoustic response due to hydrodynamic sources*, Comput. Methods Appl. Mech. Engrg., Vol. 190, pp. 345-361 (2000).

[32] ParaView©, *Data analysis and visualization software*, Sandia Corporation, Sandia National Laboratories, New Mexico PO Box 5800 Albuquerque, NM 87185 and Kitware, Inc., 28 Corporate Drive, Clifton Park, New York 12065 USA.

[33] Sandboge R., Caro S., Ploumhans P., Ambs R., Schillemeit B. and Shakib F., *Validation of a CAA formulation based on Lighthill's analogy using AcuSolve and Actran/LA on an idealized automotive HVAC blower and on an axial fan*, AIAA/CEAS 12th Aeroacoustic Conference, 8-10 May 2006, Cambridge, Massachusetts, USA (2006).

[34] Sandboge R., Washburn K. and Peak C., *Validation of a CAA formulation based on Lighthill's analogy for a cooling fan and mower blade noise*, Fan Noise 2007 Conference, 17-19 September 2007, Lyon, France (2007).

[35] Shirron J.J., *Solution of Exterior Helmholtz Problems Using Finite and Infinite Elements*, Ph.D. Thesis, College Park: University of Maryland (1995).

[36] Thompson L.L. and Pinsky P.M., *A Galerkin/least-squares finite element method for the two-dimensional Helmholtz equation*, Int. J. Numer. Methods Engrg., Vol. 38, pp. 371-397 (1995).

[37] Thompson L.L., *A review of finite-element methods for time-harmonic acoustics*, J. Acoust. Soc. Am., Vol. 119, pp. 1315-1330 (2006).

[38] White F.M., *Viscous Fluid Flow*, 2nd ed., McGraw-Hill (1991).

[39] Wilcox C.H., *An expansion theorem for electromagnetic fields*, Commun. Pure Appl. Math., Vol. 9, pp. 115-134 (1956).

[40] Wolfram Mathematica®, *Computational software*, Wolfram Research, Inc., 100 Trade Center Drive, Champaign, IL 61820-7237, USA.

[41] Yang Y., *Generation of Tones Due to Grazing Shear Flow Past a Deep Cavity*, Ph.D. Thesis, Lehigh University (2005).

[42] Yang Y., Rockwell D., Lai-Fook Cody K. and Pollack M., *Generation of tones due to flow past a deep cavity: Effect of streamwise length*, J. Fluid Struct., Vol. 25, pp. 364-388 (2009).